

THESIS FOR THE DEGREE OF LICENTIATE OF ENGINEERING

Engineering Epitaxial Graphene for Quantum Metrology

Uniform, stable and tuneable chemical doping

HANS HE

Department of Microtechnology and Nanoscience (MC2)  
Quantum Device Physics Laboratory  
CHALMERS UNIVERSITY OF TECHNOLOGY

Göteborg, Sweden 2018

Engineering Epitaxial Graphene for Quantum Metrology  
Uniform, stable and tuneable chemical doping  
HANS HE

ISSN 1652-0769  
Technical Report MC2-396

© HANS HE, 2018

Department of Microtechnology and Nanoscience (MC2)  
Quantum Device Physics Laboratory  
Chalmers University of Technology  
SE-412 96 Göteborg  
Sweden  
Telephone: +46 (0)31-772 1000

Cover:

False-color optical image of a 10  $\mu\text{m}$  wide epitaxial graphene Hall bar device on a silicon carbide substrate. The lighter blue stripe is graphene, while the darker blue is silicon carbide. Six gold contact leads, yellow color, allow for electrical characterization of the device. The lines running parallel to the Hall bar are nanometer-sized steps on the substrate.

Chalmers Reproservice  
Göteborg, Sweden 2018

Engineering Epitaxial Graphene for Quantum Metrology

Uniform, stable and tuneable chemical doping

Thesis for the degree of Licentiate of Engineering

HANS HE

Department of Microtechnology and Nanoscience (MC2)

Quantum Device Physics Laboratory

Chalmers University of Technology

## ABSTRACT

Quantum resistance metrology deals both with the precise and accurate measurement of electrical resistance, by utilizing the quantum hall effect (QHE) in two-dimensional electron gases (2DEGs) such as those based on gallium arsenide (GaAs). Due to the unique properties of graphene, and specifically epitaxial graphene grown on silicon carbide (SiC/G), quantum Hall resistance (QHR) standards based on graphene perform better in a wider parameter space (temperature, current and magnetic field) than conventional semiconducting materials. To date, this is possibly the only real-world application of graphene. However, due to the nature of SiC/G there are still certain issues than remain unsolved, which stand in the way for widespread use of graphene QHR devices. This work aims to discuss, and suggest solutions to, one of the major problems: charge carrier density control.

Control over the charge carrier density is crucial in order to observe the quantum Hall effect at sufficiently low magnetic fields. Since SiC/G is intrinsically n-doped ( $n \approx 10^{13} \text{ cm}^{-2}$ ) due to interactions with the SiC substrate, external doping methods must be used in order to bring graphene closer to charge neutrality. Previous techniques such as photochemical gating [1], corona discharge of ions [2] or electrostatic gating [3] lack either potency, stability or tuneability. This thesis presents an air-stable chemical gating method using the acceptor molecule 2,3,5,6-Tetrafluoro-tetracyanoquinodimethane (F4TCNQ) mixed with a poly(methyl-methacrylate) (PMMA) polymer. This dopant blend can be applied to SiC/G using simple spin coating, forgoing the need for ultra-high vacuum (UHV) systems. It provides potent and homogeneous doping, with the ability to bring SiC/G close to charge neutrality, with measured mobilities reaching  $70,000 \text{ cm}^2/\text{Vs}$ . Furthermore, the method is compatible with macroscopic devices with the doping being significantly homogeneous even on the millimeter scale. Chemical analysis reveal that the doping effect is a consequence of F4TCNQ molecules diffusing through the PMMA matrix and preferentially assembling near the graphene surface. Charge transfer and doping is attributed to the formation of a charge-transfer complex between F4TCNQ and graphene. The low carrier densities and high carrier mobilities for chemically doped samples is the result of low charge disorder ( $\pm 6 \times 10^9 \text{ cm}^{-2} \approx \pm 9 \text{ meV}$ ), thus far only attainable in state-of-the-art exfoliated graphene flakes encapsulated by hexagonal boron nitride (hBN) [4] or suspended graphene [5]. Initial measurements performed at metrological institutes, comparing SiC/G to GaAs, suggest that the chemical dopant is compatible with precision measurements of quantized resistance  $h/2e^2$  on the order of  $n\Omega/\Omega$ .

Keywords: Epitaxial Graphene, Chemical Doping, Magnetotransport, Quantum Resistance Metrology



*Dedicated to my beloved Lan Huong*



## ACKNOWLEDGEMENTS

To begin with, I would like to thank my supervisor Sergey Kubatkin for accepting me into his group. I have always felt at home in our little research community, and I thank you for giving me the opportunity to contribute to the group's success and to develop as a researcher. Your leadership, wisdom and experience have been invaluable to me and my work. Furthermore, I wish to thank my co-supervisor Samuel Lara for dedicating much of his time coaching and supporting me throughout the years. I am grateful for your patience and hard work. Without your expertise and guidance I would be lost, and I owe much of my knowledge about experimental physics to you. I would also like to thank the rest of our group members, current and past, Andrey Danilov, Kyung Ho Kim, Domenico Montemurro, Astghik Adamyan, Tom Yager, and Arseniy Lartsev for many fruitful discussions and your willingness to help with any experiments, big or small. A thanks to our previous master's students Maria Karani, Mohab O. Hassan, and David Barker for their contributions to this work.

Many thanks to my co-supervisor at RISE, Tobias Bergsten, for being my guide in the world of metrology and opening my eyes to the world of uncertainties and error. You have shed light on the intricacies of precision measurements with part-per-billion accuracy. Special thanks to Gunnar Eklund for your assistance in the labs at RISE.

Most of the work in this thesis was done in the wonderful clean room and labs here at Chalmers. Working there is always a pleasure and it is thanks to the dedicated clean room staff that the machines are working as smoothly as they are. Special thanks to Niclas Lindvall, Alexei Kalaboukhov, Mats Hagberg, Henrik Fredriksen, Johan Andersson, and Ulf Södervall for their continued support. I would also like to extend thanks to Lars Jönsson for his excellent work in the workshop. Special thanks to Grigory Skoblin and August Yurgens for their help with hBN encapsulation.

Thanks to the wonderful co-workers and friends here at MC2 who make this environment a fun and productive place. Special thanks to my friend and office-mate Lu Yong for greatly improving my skills in chinese. Marco Scigliuzzo for many interesting discussions about physics and politics, and also for making delicious tiramisu. Patric Holmvall for endless entertainment and jolly cooperation.

Finally, I would like to thank my family and friends for supporting me all these years. You have kept me going even when things get tough.



## ABBREVIATIONS

2D	Two-dimensional
2DEG	Two-dimensional electron gas
AFM	Atomic force microscopy
C-face	Carbon face of silicon Carbide
CVD	Chemical vapor deposition
DOS	Density of states
EBL	Electron beam lithography
F4TCNQ	2,3,5,6-Tetrafluoro-tetracyanoquinodimethane
GaAs	Gallium arsenide
GIWAXs	Grazing-incidence wide-angle x-ray scattering
hBN	Hexagonal boron nitride
IPA	Isopropanol
LL	Landau level
PMMA	Poly(methyl-methacrylate)
QHE	Quantum Hall effect
QHR	Quantum Hall resistance
SEM	Scanning electron microscopy
SiC	Silicon carbide
SiC/G	Epitaxial graphene on silicon carbide
Si-face	Silicon face of silicon carbide
SIMS	Secondary-ion mass spectroscopy
UHV	Ultra-high vacuum
vdW	van der Waals

## SYMBOLS

$\alpha$	Fine Structure Constant
$k_B$	Boltzmann Constant
$h$	Planck Constant
$e$	Elementary Charge
$c$	Speed of Light in Vacuum
$n$	Charge Carrier Density
$n_e$	Electron Charge Carrier Density
$n_h$	Hole Charge Carrier Density
$B$	Magnetic Field
$T$	Temperature
$t$	Time
$I$	Current
$V$	Voltage
$l_B$	Magnetic length
$V_G$	Gate Voltage
$E_F$	Fermi Energy
$v_F$	Fermi Velocity
$\mu$	Charge Carrier Mobility
$\tau$	Transport time
$R_H$	Hall Coefficient
$\nu$	Filling factor
$\rho_{XX}$	Longitudinal Hall Sheet Resistance
$R_{XX}$	Longitudinal Hall Resistance
$R_{XY}$	Transverse Hall Resistance

# THESIS

This thesis consists of an extended summary and the following appended papers:

**Paper A** H. He, T. J.B. M. Janssen, S. Rozhko, A. Tzalenchuk, S. Lara-Avila, R. Yakimova, and S. Kubatkin. Fabrication of graphene quantum hall resistance standard in a cryogen-table-top system. *2016 Conference on Precision Electromagnetic Measurements (CPEM 2016)* (2016), 1–2

**Paper B** H. He, K. H. Kim, A. Danilov, D. Montemurro, L. Yu, Y. W. Park, F. Lombardi, T. Bauch, K. Moth-poulsen, T. Iakimov, R. Yakimova, P. Malmberg, C. Müller, S. Kubatkin, and S. Lara-Avila. Uniform doping of graphene close to the charge neutrality point by polymer-assisted spontaneous assembly of molecular dopants. *Manuscript under consideration in Nature Materials* (2018), arXiv:1805.05644

Other publications related to thesis

**Paper I** T. J.B. M. Janssen, S Rozhko, I Antonov, A Tzalenchuk, J. M. Williams, Z Melhem, H He, S Lara-Avila, S Kubatkin, and R Yakimova. Operation of graphene quantum Hall resistance standard in a cryogen-free table-top system. *2D Materials* **2**.3 (2015), 035015

**Patent I** H. He, S. Lara-Avila, and S. Kubatkin . *Assembling of molecules on a 2D material and an electronic device.* Swedish Patent and Registration Office. 1751625-3. Patent pending 2017.

**Patent II** H. He, S. Lara-Avila, and S. Kubatkin. *Electrical contacts for low dimensional materials.* Swedish Patent and Registration Office. 1850366-4. Patent pending 2018.



# CONTENTS

<b>Abstract</b>	i
<b>Acknowledgements</b>	v
<b>Abbreviations</b>	vii
<b>Symbols</b>	viii
<b>Thesis</b>	ix
<b>Contents</b>	xi
<b>1 Introduction</b>	1
1.1 Outline . . . . .	3
<b>2 Theory and Concepts</b>	5
2.1 Magnetotransport . . . . .	5
2.1.1 Single Band Hall Effect . . . . .	6
2.1.2 Integer Quantum Hall Effect . . . . .	8
2.2 Graphene . . . . .	11
2.2.1 Electronic Properties . . . . .	12
2.2.2 Two Band Hall Effect . . . . .	16
2.2.3 Half-integer Quantum Hall Effect . . . . .	17
2.2.4 Epitaxial Graphene on Silicon Carbide . . . . .	19
<b>3 Experimental Methods</b>	21
3.1 Graphene Growth . . . . .	21
3.1.1 Optical Microscopy . . . . .	22
3.1.2 Atomic Force Microscopy . . . . .	23
3.1.3 Raman Spectroscopy . . . . .	25
3.2 Microfabrication . . . . .	25
3.3 Chemical Doping . . . . .	27
3.3.1 Secondary-ion Mass Spectroscopy . . . . .	28
3.3.2 Gracing-incidence Wide-angle X-ray Scattering . . . . .	28
3.4 Electrical Characterization . . . . .	29
3.4.1 Cryogenic Current Comparator . . . . .	30
<b>4 Results and Discussion</b>	33
4.1 Table-top System . . . . .	33
4.2 Chemical Doping . . . . .	34
4.2.1 Towards charge neutrality . . . . .	34
4.2.2 Spontaneous Assembly . . . . .	36
4.2.3 Tuning Doping via Thermal Annealing . . . . .	39

4.2.4	Macroscopic Homogeneity . . . . .	41
4.2.5	Microscopic Homogeneity . . . . .	42
4.2.6	Grazing-incidence Wide-angle X-ray Scattering . . . . .	46
4.2.7	Redistribution of Dopants . . . . .	47
4.3	Initial Metrological Tests . . . . .	50
<b>5</b>	<b>Conclusions and Outlook</b>	<b>54</b>
<b>A</b>	<b>Recipes</b>	<b>57</b>
A.1	RCA cleaning . . . . .	57
A.2	Electron Beam Lithography . . . . .	57
A.2.1	Anchors . . . . .	57
A.2.2	Contacts . . . . .	58
A.2.3	Ashing . . . . .	59
A.3	Chemical Doping . . . . .	59
A.3.1	Dopant blend . . . . .	59
A.3.2	Spin coating . . . . .	59
<b>References</b>		<b>60</b>
<b>I</b>	<b>Appended Papers A</b>	<b>65</b>
<b>II</b>	<b>Other Publications</b>	<b>99</b>

# 1 Introduction

Graphene is a truly two-dimensional material, consisting of a single layer of carbon atoms arranged in a hexagonal lattice. Its crystal structure leads to unique properties which, in many cases, exceed those found in conventional semiconducting materials. For instance, graphene is a zero-gap semi-metal, with effectively massless charge carriers, and possesses record-high electron mobilities at room temperature [6]. Graphene displays broad band absorption of light proportional to the fine structure constant  $\alpha$  [7], absorbing 2.3 % of light while being only one atom thick. Thermal conductivity reportedly up to 3000 W/mK, which is comparable to copper [8]. Mechanical properties include being flexible and lauded as the strongest material in the world (for its size) [9].

This wondrous material was theoretically studied by Wallace as early as 1947 [10], but it was not until its experimental isolation and verification by Geim and Novoselov in 2004 [11, 12] that graphene captured the attention of researchers across the world. Graphene has been envisioned to usher in new technological innovations and surpass currently technologies in various fields such as bio-medicine, composite materials, gas sensors, energy harvesting and storage, and various electronics. Thus far, efforts to surpass currently technologies have been difficult. One, and perhaps the only, electrical application that utilizes the unique electrical properties of graphene that exists today is within the area of quantum resistance metrology.

Quantum resistance metrology deals with the definition and precise measurement of the unit of resistance Ohm ( $\Omega$ ). This line of work demands high precision measurements with measurement uncertainties on the order of  $n\Omega/\Omega$ , or better. Traditionally, quantum resistance metrology relies on the quantum hall effect (QHE) [13] observed in two-dimensional electron gases (2DEG) such as those based on gallium arsenide (GaAs). In these systems, when the sample is sufficiently cooled ( $<1$  K) and subjected to an out-of-plane magnetic field ( $>10$  T), the transverse resistance ( $R_{XY}$ ) takes on well-defined values related to only fundamental constants Planck's constant  $h$  and elementary charge  $e$ . These quantized values of resistance are proportional to  $R_K = h/e^2$ , aptly named the von Klitzing constant, after the discoverer of QHE. Since the quantized value of resistance depend only on fundamental constants, it provides an excellent reference point for resistance measurements and calibrations. The universality of the QHE ensures that in principle any sample can be used as the primary realization of electrical resistance, forgoing the need for artifact standards [14]. Due to the unique properties of graphene, and specifically epitaxial graphene grown on silicon carbide (SiC/G), the QHE can be observed in graphene at higher temperatures, lower magnetic fields, and at higher bias currents than for conventional 2DEGs [15–17]. In addition, the quantum hall plateau corresponding to filling factor  $\nu=2$  is very robust in graphene, extending to 50 T [18]. SiC/G is also attractive because it is a scalable technology, enabling wafer-sized growth of high-quality graphene [19]. SiC/G based quantum hall resistance (QHR) standards are therefore not only the superior realization of electrical resistance, but also the key component which enable the primary standard to be brought closer to the end-user. Due to more relaxed measurement conditions, a graphene based QHR does not necessarily need high-end equipment or state-of-the-art laboratories to function, and work towards a table-top, cryogen-free, version of graphene QHR has already been made [17]. However,

there are still unresolved issues regarding the fabrication and preparation of graphene QHR standards, which limit the performance and reliability of devices. This work presents a solution to one of the main culprits: charge carrier density control.

Due to the nature of the growth of SiC/G, there is an interface layer of carbon, also known as buffer layer, which in conjunction with the SiC substrate heavily n-dope SiC/G, on the order of  $n \approx 10^{13} \text{ cm}^{-2}$  [20]. This high charge carrier density increases the minimum required magnetic field in order to reach quantizing conditions, thus for practical reasons the charge carrier concentration needs to be decreased using external doping methods. Another consideration is related to critical currents, which should be maximized in order to boost signal-to-noise-ratio and decrease the measurement uncertainty to  $n\Omega/\Omega$  or below. For a specific set of operating conditions (magnetic field and temperature) there is an optimum charge carrier concentration which maximizes critical current [17]. Therefore, one need not only to lower the charge carrier density but also to be able to tune it. Ideally, for real-world applications, the charge carrier density should also possess long-term stability. Another consideration is that the method should be scalable and compatible with wafer-scale technology, like SiC/G already is. Finally, the stability and accuracy of the quantized resistance plateau is sensitive to charge disorder [21, 22] which puts constraints on the homogeneity of doping, and quality of graphene itself.

There already exist many methods to tune the carrier density of SiC/G, however they all lack either potency, stability or tunability. Photochemical gating [1], which utilizes UV exposure of poly(methyl styrene-chloromethyl acrylate), lacks the potency to tune the density more than  $\approx 3 \times 10^{12} \text{ cm}^{-2}$ . Corona discharge of ions [2] is much more potent but is volatile at ambient conditions. Due to the high density of states in the intrinsic buffer layer effectively pinning the Fermi level of graphene, the geometric capacitance of an electrostatic gating (or any gating effect) is reduced by an order of magnitude [20], making the high intrinsic n-doping even more problematic.

This thesis summarizes and elaborates upon the work of **Paper A**, **Paper I**, and **Paper B**. **Paper A** and **Paper I** sets the stage and introduces work done in order to achieve a practical realization of SiC/G based QHR standards, with the goal of operating with metrological precision at 4.2 K and below 5 T. The difficulty in tuning the charge carrier density for SiC/G motivated the work done in **Paper B**, which is the main result of this thesis. **Paper B** demonstrates a novel way to dope graphene using a chemical method based on the acceptor molecule 2,3,5,6-Tetrafluoro-tetracyanoquinodimethane (F4TCNQ) integrated in a polymer matrix of poly(methyl-methacrylate) (PMMA). Chemical doping of graphene using directly deposited F4TCNQ has been explored previously [23, 24], but macroscopic electrical transport was complicated by instability at ambient conditions. The addition of PMMA as a host for the F4TCNQ molecules results in a method which provides tuneable, strong, and stable doping of SiC/G, with the possibility of bringing SiC/G close to charge neutrality. The resulting system is also interesting from a fundamental research point of view, since F4TCNQ molecules are observed to be capable of diffusing through the PMMA and spontaneously assembling close to the surface of graphene. The formation of a charge-complex between F4TCNQ molecules and graphene results in not only p-doping, but spatially homogeneous doping with low charge disorder  $\approx 9 \text{ meV}$ , comparable to that of hBN encapsulated graphene flakes [4] or suspended graphene [5].

## 1.1 Outline

Chapter 2 introduces concepts and theory regarding electron transport under the influence of a magnetic field. It starts with classical and quantum transport for normal 2DEG systems, before moving on to how the physics change for monolayer graphene. The chapter ends with a brief discussion about the peculiarities of SiC/G.

Chapter 3 contains descriptions of the experimental methods. It includes growth of SiC/G, microfabrication, electrical measurements and chemical doping. In addition, several useful non-electrical characterization methods such as optical microscopy, atomic force microscopy (AFM), Raman spectroscopy, secondary-ion mass spectroscopy (SIMS) and grazing-incidence wide-angle x-ray scattering (GIWAXs) are discussed.

Chapter 4 presents the experimental results of this thesis. It begins with a brief introduction to previous work related to a table-top QHR standard (**Paper A**, **Paper I**) which serves as the starting point and driving force behind investigations into charge carrier density control of SiC/G. The second section deals with the main result of this thesis, presented in **Paper B**, which is F4TCNQ doping of SiC/G, guided by a PMMA polymer matrix. Finally, initial metrological tests of the doping method are presented (to be published).

Chapter 5 is the final and concluding chapter. The main findings are summarized and future prospects are discussed.



## 2 Theory and Concepts

This chapter will provide an introduction to the theory and concepts behind the electrical properties of graphene, and specifically epitaxial graphene on silicon carbide. The first section will discuss general magnetotransport phenomena in two dimensions (2D) and the second section will focus graphene itself. For a more in-depth look consult [25, 26] for general electron transport theory and [27–29] for graphene specific theory.

### 2.1 Magnetotransport

A simple classical model of the transport of electrons through a material is given by the Drude model, wherein electrons are considered to be independent particles, moving around the solid like molecules in a gas. Interactions with other electrons and the lattice ions have been collected into the effective mass of electrons  $m^*$ , thus the electrons are treated as free electrons, albeit with a different mass. The electrons travel freely throughout the lattice until they encounter a scattering center, such as an ion, and the collision results in an instantaneous change of momentum. The mean travel distance before such a collision is called the mean free path  $\lambda$  and it is through these collisions that electrons reach thermal equilibrium with their surroundings.

The electrons can be accelerated by magnetic and electric fields, as is the case during magnetotransport measurements. The resulting force is called the Lorentz force and is expressed as Equation 2.1, where  $q$  is the charge (-e for electrons),  $\mathbf{E}$  is the electric field,  $\mathbf{B}$  is the magnetic field and  $\mathbf{v}_I$  is the instantaneous velocity of the electron.

$$\mathbf{F} = q(\mathbf{E} + \mathbf{v}_I \times \mathbf{B}) \quad (2.1)$$

Note that while the electric field accelerates electrons parallel to the field direction, the magnetic field deflects the path of the electrons perpendicular to both the field and the instantaneous velocity. For instance, for an electron moving in a 2D system an out-of-plane magnetic field will cause the electron to have a circular trajectory. As electrons move around under the influence of the Lorentz force they also undergo collisions at a rate of  $1/\tau$ . For the electrons which suffer a collision, the total effect of their individual collisions can be estimated by a frictional damping force  $-m^*\mathbf{v}/\tau$ . At thermal equilibrium the electrons will have acquired an average drift velocity  $\mathbf{v}$ , where the drift velocity is the net velocity acquired due to external influence (normally electrons will move around randomly at the Fermi velocity  $v_F$ ). The drift velocity is given simply by Newton's equation  $F = ma$  as:

$$q(\mathbf{E} + \mathbf{v} \times \mathbf{B}) - m^* \frac{\mathbf{v}}{\tau} = m^* \left( \frac{d\mathbf{v}}{dt} \right) \quad (2.2)$$

The steady state solution, where  $d\mathbf{v}/dt = 0$ , in 2D (x-y plane), with the magnetic field

being out-of-plane (z-direction), is given by solving:

$$\begin{aligned} 0 &= -eE_X - eBv_Y - m^* \frac{v_X}{\tau} \\ 0 &= -eE_Y + eBv_X - m^* \frac{v_Y}{\tau} \end{aligned} \quad (2.3)$$

The convention here uses X and Y to denote components along x or y direction respectively. The current density  $\mathbf{J}$  is related to the drift velocity as  $\mathbf{J} = qn\mathbf{v}$  were n is the charge carrier density. Equation 2.3 can then be transformed into:

$$\begin{aligned} \sigma_0 E_X &= \omega_c \tau J_Y + J_X \\ \sigma_0 E_Y &= -\omega_c \tau J_X + J_Y \end{aligned} \quad (2.4)$$

$\sigma_0 = ne^2\tau/m^*$  is the DC Drude conductivity in the absence of magnetic field.  $\omega_c = eB/m^*$  is the cyclotron frequency, which is a measure of how fast electrons complete one cyclotron orbit due to the magnetic field. Without an external magnetic field Equation 2.4 simply states  $E = J/\sigma_0$ , which is the famous Ohm's Law. Additionally, the conductivity can be expressed as  $\sigma_0 = en\mu$ . The mobility  $\mu$  is the proportionally constant which relates the drift velocity to the applied electrical field  $\mathbf{v} = \mu\mathbf{E}$ , a higher mobility figure  $\mu = e\tau/m^*$  means in general higher quality material, for instance due to decreased number of scattering centers.

Equation 2.4 can be expressed in matrix form as:

$$\mathbf{E} = \rho \mathbf{J} = \begin{pmatrix} \rho_{XX} & \rho_{XY} \\ -\rho_{XY} & \rho_{YY} \end{pmatrix} \mathbf{J} = \sigma_0^{-1} \begin{pmatrix} 1 & \omega_c \tau \\ -\omega_c \tau & 1 \end{pmatrix} \mathbf{J} \quad (2.5)$$

$\rho$  signifies sheet resistance which for the longitudinal case is  $\rho_{XX} = R_{XX}W/L$  where W is the width of the Hall bar and L the length (see Figure 2.1) and  $R_{XX} = V_X/I_X$ . In the transverse case  $\rho_{XY} = R_{XY} = V_Y/I_X$ , the resistance and resistivity are one and the same. Inverting the resistivity tensor results in the conductivity tensor:

$$\sigma = \frac{\sigma_0}{1 + \omega_c^2 \tau^2} \begin{pmatrix} 1 & -\omega_c \tau \\ \omega_c \tau & 1 \end{pmatrix} \quad (2.6)$$

The conductivity, under the influence of a magnetic field, is then:

$$\begin{aligned} \sigma_{XX} &= \frac{\rho_{XX}}{\rho_{XX}^2 + \rho_{XY}^2} \\ \sigma_{XY} &= \frac{-\rho_{XY}}{\rho_{XX}^2 + \rho_{XY}^2} \end{aligned} \quad (2.7)$$

### 2.1.1 Single Band Hall Effect

Figure 2.1 depicts electrons traveling across a rectangular 2D conductor in the x-direction (longitudinal). Subjected to a magnetic field perpendicular to the plane of the Hall bar, the Lorentz force deflects them to one side of the Hall bar. This charge build-up leads to an electric field, or Hall voltage, which counteracts the force from the magnetic field. In

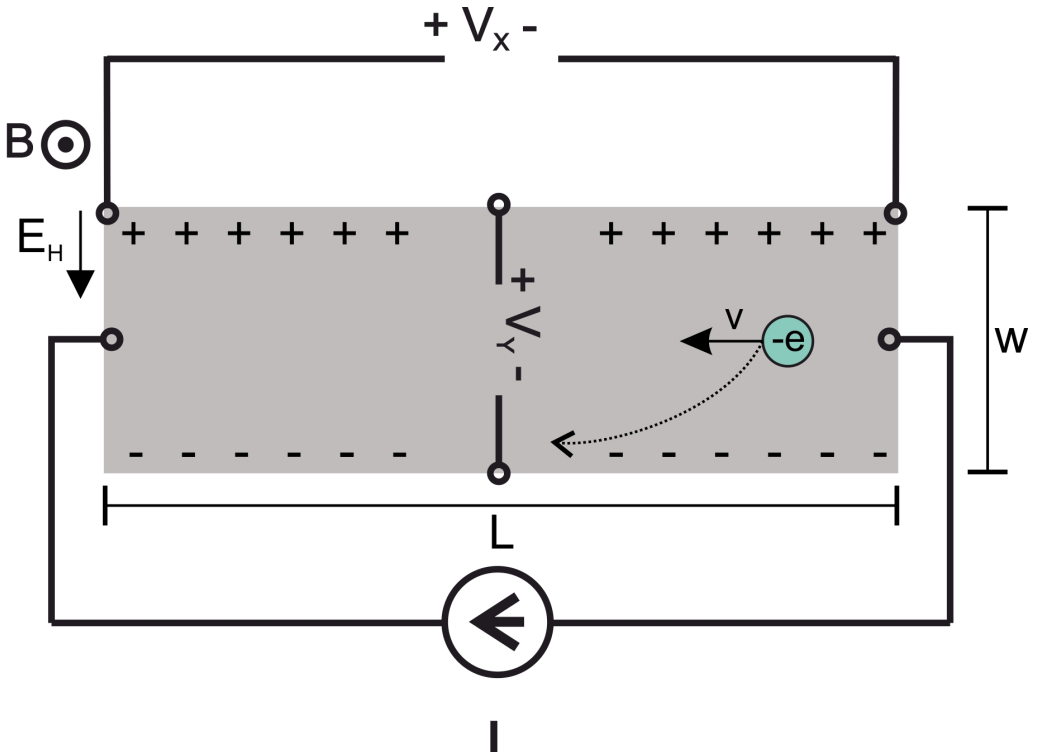


Figure 2.1: Schematic representation of the Hall effect measured in a 2D Hall bar sample. The sample has width  $W$  and length  $L$ . As electrical current is passed from one end of the Hall bar to the other, a longitudinal voltage  $V_X$  can be measured. If a magnetic field is applied perpendicular to the plane of the Hall bar the electrons experience a force perpendicular to their motion and their trajectories are deflected to one side of the Hall bar. This causes charge separation and a charge build-up which causes an internal electric field  $E_H$  to appear. The force from the field  $E_H$  opposes the force from the magnetic field  $B$  and at equilibrium the force from the magnetic field and electric field exactly cancel. The measured transverse voltage  $V_Y$  is then the Hall voltage. The situation is analogous for holes, with the exception that the Hall voltage changes sign.

equilibrium there is no longer any current in the  $y$ -direction (transverse). Setting  $J_Y = 0$  in Equation 2.4:

$$\begin{aligned} \sigma_0 E_Y &= -\omega_c \tau J_X \\ \Rightarrow E_Y &= -\frac{\omega_c \tau}{\sigma} J_X = -\frac{1}{ne} J_X B \end{aligned} \tag{2.8}$$

Defining  $R_H = E_Y / J_X B$  as the Hall coefficient (in practice  $R_H = dR_{XY} / dB$ ) yields

the expression:

$$R_H = -\frac{1}{ne} \quad (2.9)$$

Equation 2.9 is used for low-field measurements, where  $R_{XY}$  is linear with magnetic field, to determine the charge carrier density  $n$ . The sign of  $R_H$  also reveals if the transport is electron-type or hole-type. Similarly, a Hall measurement can also determine the mobility:

$$\mu = \frac{\sigma_0}{en} = \frac{-R_H}{\rho_{XX,B=0}} \quad (2.10)$$

Here  $\rho_{XX}$  is the sheet resistance, at zero magnetic field.

### 2.1.2 Integer Quantum Hall Effect

From Equation 2.4 the transverse resistance  $R_{XY}$  is always linear with magnetic field, while the longitudinal resistance  $R_{XX}$  is constant with magnetic field. This due to limitations of the classical model. In reality for 2D systems, at sufficiently low temperatures and with high carrier mobility, stronger magnetic fields give rise to quantum mechanical phenomena such as Shubnikov-De Haas oscillations and quantum Hall effect (QHE). Shubnikov-De Haas oscillations manifests themselves as oscillations in longitudinal resistance  $R_{XX}$  with  $1/B$  periodicity [30]. The quantum Hall effect manifests itself as quantized values of transverse resistance, proportional to  $R_K = h/e^2$  where  $h$  is Planck constant and  $e$  elementary charge. These quantized values of resistance form plateaus in magnetic field, in which the resistance is constant. While the  $R_{XY}$  is quantized and on such a plateau in field, the longitudinal resistance vanishes  $R_{XX} = 0$ .

Both of the aforementioned phenomena share the same origin, which is the formation of Landau levels (LLs) in the electronic density of states at higher magnetic fields. This is a consequence of the cyclotron orbits of the electrons being quantized, i.e. they are only allowed to take on specific values. The LLs are formally calculated by solving the Schrödinger equation for free electrons subjected to a magnetic field. The quantum Hamiltonian is:

$$H = \frac{1}{2m}(\mathbf{p} + e\mathbf{A})^2 \quad (2.11)$$

The vector potential  $\mathbf{A}$  represents the magnetic field. Assume that the 2D systems exists in the  $x$ - $y$  plane, then for an out-of-plane perpendicular field in the  $z$ -direction  $\nabla\mathbf{A} = B\hat{\mathbf{z}}$ . There is freedom to choose a gauge and the Landau gauge is used  $\mathbf{A} = xB\hat{\mathbf{y}}$ . The Hamiltonian now reads (coordinate basis orthonormal):

$$H = \frac{1}{2m}(p_x^2 + (p_y + eBx)^2) \quad (2.12)$$

Due to the choice of gauge only the  $y$ -direction has translational invariance. The energy eigenstates which also are eigenstates of  $p_y$  are plane waves in the  $y$ -direction. Using the separation of variables ansatz for the wavefunction  $\Psi_k(x, y) = e^{iky}f_k(x)$  means that

the operator  $p_y = -i\hbar \frac{\partial}{\partial y}$  simply gets replaced by the eigenvalue  $\hbar k$  in the Schrödinger equation:

$$H\Psi_k(x, y) = \frac{1}{2m}(p_x^2 + (\hbar k + eBx)^2)\Psi_k(x, y) \quad (2.13)$$

The Hamiltonian can be rewritten as:

$$H = \frac{1}{2m}p_x^2 + \frac{m\omega_c^2}{2}(x + kl_B^2)^2 \quad (2.14)$$

This Hamiltonian is identical to that of the quantum harmonic oscillator with the difference that the potential minimum is shifted by  $-kl_B^2$  where  $l_B = \sqrt{\frac{\hbar}{eB}}$ .  $l_B$  is called the magnetic length, and it is a characteristic length scale of quantum interactions in a magnetic field, closely related to the minimum radius of cyclotron orbits allowed by the Heisenberg uncertainty principle. The eigenenergies for any quantum harmonic oscillator is  $E_n = \hbar\omega_c(N + \frac{1}{2})$ ,  $N \in \mathbb{N}^0$  and the energy spacing between LLs is therefore equidistant.

The LL are highly degenerate, and contain many states. For a system with charge carrier density  $n$ , the number of filled LLs, called the filling factor  $\nu$ , is simply  $\nu = n/n_L$  where  $n_L$  refers to the number of electrons required to completely fill one LL. An upper bound of the LL degeneracy is given if each localized electron in the LL encircles a single flux quantum  $\Phi_0 = h/e$ . The number of electrons in the LL, per unit area  $A$ , is then a function of the applied magnetic field (flux density)  $n_L = B/\Phi_0$ .

Armed with the knowledge of the degeneracy of LLs it is easy to see why the transverse resistance  $R_{XY}$  is quantized. From the Drude model and Equation 2.9 the transverse resistance is dependent on the charge carrier density  $R_{XY} = B/ne$ . Simply plugging in  $n = \nu n_l = \nu B/\Phi_0$  yields:

$$R_{XY} = \frac{h}{\nu e^2}, \nu \in \mathbb{Z} \quad (2.15)$$

To experimentally observe the quantum Hall effect the charge carrier density is kept constant while magnetic field is swept, as seen in Figure 2.2 (alternatively the charge carrier density can be varied with a gate while keeping magnetic field constant). As the magnetic field is increased the higher LLs are emptied, and as each one is emptied the transverse resistance increases. The quantization of resistance expressed in Equation 2.15 only occurs when exactly  $\nu$  LLs are filled. However, experimentally it is observed that when the Fermi energy lies between two LLs there is an existence of plateaus in magnetic field, and this is called the quantum Hall regime. These plateaus are attributed to broadening of the LLs due to disorder (small enough as to not cause overlap of LLs). For a pristine sample the LLs are delta functions in the density of states, and no plateaus are observed. The presence of disorder splits the degeneracy of the LLs causing broadening in energy, and creates localized and extended states at each LL. The localized states do not contribute to conduction, while extended state do. The extended states appear close to the center of the LL, while the localized states exist to the sides. Thus, as magnetic field is swept the localized states are affected (emptied/filled) first, and do not affect conduction, resulting in the plateaus of constant resistance in magnetic field.

The spatial location of localized and extended states are of interest, especially to understand why  $\rho_{XX} = 0$  in the quantum hall regime. Consider a real Hall bar sample

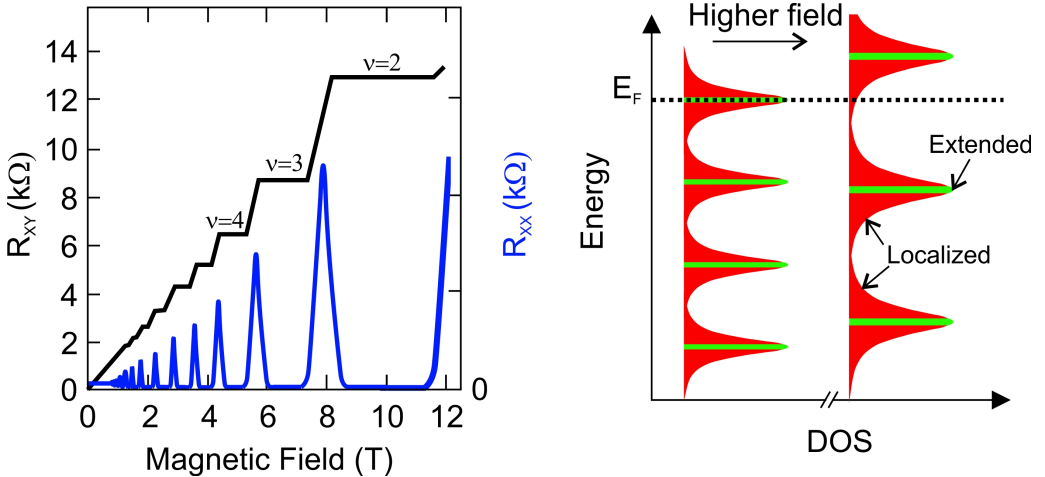


Figure 2.2: **Left:** Schematic representation of the evolution of transverse resistance  $R_{XY}$  and longitudinal resistance  $R_{XX}$  as one increases magnetic field. At low fields, the behavior is classical with linear  $R_{XY}$  and constant  $R_{XX}$ . At slightly higher magnetic fields  $R_{XY}$  starts to develop resistance plateaus while  $R_{XX}$  tends to zero at each plateau. The quantization is not perfect yet because the overlap between LLs is still too large. For even higher magnetic fields the system enters fully into the quantum Hall regime, with exactly quantized plateaus and zero longitudinal resistance. As the magnetic field is increase further, the higher energy LLs are successively emptied leading to the steps in  $R_{XY}$  and oscillations between finite and zero resistance in  $R_{XX}$ . **Right:** Schematic representation of the density of states showing the LLs with lorentzian broadening due to disorder. The red region denote localized states, which do not contribute to conduction. The green region are the extended states which do conduct. The energy spacing (and degeneracy) of the LLs increases as the magnetic field increases, and since the Fermi energy is fixed, the effect is that more and more LLs are emptied as the field increases. The plateau in  $R_{XY}$  and zero resistance  $R_{XX}$  occur when the Fermi energy sits between two LLs, where only localized states exist. The slope in  $R_{XY}$  and peak in  $R_{XX}$  occur when the Fermi level passes through the center of a LL as it is emptied of extended states

which has finite dimensions and edges at the boundary as in Figure 2.3. Ignoring spatial variations of the potential due to disorder, the LLs lie flat in the bulk and rise steeply at the edges, like the confining walls of a potential well. The Fermi energy lies in between two LLs, as is the case for the quantum Hall regime. Assuming that the potential at the edges is linear with distance, solving the Schrodinger equation yields the drift velocity  $v_x = -\frac{1}{eB} \frac{\delta V}{\delta x}$ . The drift velocity on opposite edges of the sample point in opposite directions, indicating chiral edge currents which are the extended states. The bulk has zero drift velocity and can be thought of consisting of localized states which do not conduct and separates the two edge channels. Each edge current can only travel in a certain direction thus suppressing back-scattering and leading to  $\rho_{XX} = 0$  when  $R_{XY}$  is on a plateau. The general picture still holds if the potential in the bulk is allowed to have

spatial variations due to disorder, as long as the variations are small enough not to cause LLs to cross each other.

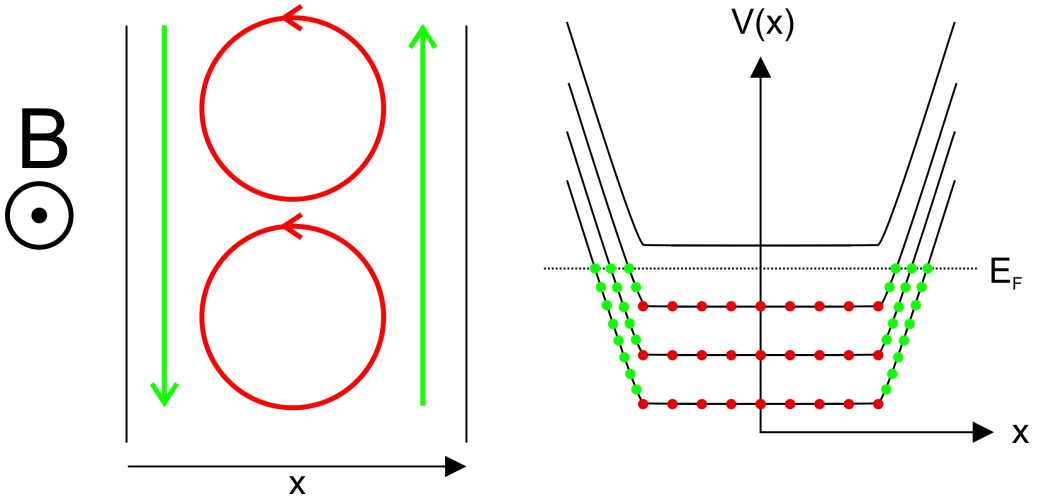


Figure 2.3: Schematic representation of the conducting edge states in quantum Hall regime. **Left:** top-down view of a Hall bar showing the directions of chiral edge currents which contribute to conductance (green), and localized bulk currents which do not (red). **Right:** Spatial variation of the potential due to LLs. In the absence of disorder the LLs are flat inside the sample. At the sample edges the potential increases rapidly to model that the electrons are confined to the Hall bar. The drift velocity is related to the derivative of the potential, thus resulting in two edge current traveling in opposite directions (green) and a localized bulk (red).

From an experimental point of view, these quantum phenomena are observable only if the electron has enough time to complete a few cyclotron orbits before scattering. This condition is fulfilled when  $1/\omega_c \ll \tau$  or equivalently  $B \gg 1/\mu$ . In order to experimentally observe QHE at reasonable fields the carrier mobility needs to be high. For reference, if the sample mobility exceeds  $\mu = 10,000 \text{ cm}^2/\text{Vs}$ , QHE can be observed at magnetic field  $B = 1 \text{ T}$ . Note that this is only a necessary but not a sufficient condition. This condition has implications for practical applications of SiC/G QHR standard in terms on sample quality, but also charge carrier density. Generally the mobility increases as charge carrier density decreases, and it is therefore desirable to be able to tune the charge carrier density, especially for SiC/G due to its high intrinsic n-doping.

## 2.2 Graphene

Graphene is a two-dimensional allotrope of carbon whose crystal structure consists of carbon atoms arranged in a hexagonal lattice. This honeycomb structure results in unique electronic properties which will be explored below. In the end of this section a few

peculiarities of SiC/G, especially relevant for investigations of QHE, will be discussed.

### 2.2.1 Electronic Properties

Figure 2.4 provides a schematic representation of the real space graphene lattice and its reciprocal counterpart. The graphene unit cell in real space is described by lattice vectors:

$$\begin{aligned}\mathbf{a}_1 &= \frac{3a_0}{2}\hat{\mathbf{x}} + \frac{\sqrt{3}a_0}{2}\hat{\mathbf{y}} \\ \mathbf{a}_2 &= \frac{3a_0}{2}\hat{\mathbf{x}} - \frac{\sqrt{3}a_0}{2}\hat{\mathbf{y}}\end{aligned}\quad (2.16)$$

where  $a$  is the distance between adjacent carbon atoms  $a_0 = 1.42$  Å and  $|\mathbf{a}_i| = a = \sqrt{3}a_0$ . The hexagonal lattice of graphene can be thought of as a combination of two triangular sublattices, A and B. The primitive cell has two carbon atoms, one from each sublattice. The symmetry between the two sublattices permeates all of the electronic properties of graphene. The planar structure of graphene is due to  $sp^2$  hybridization of orbitals between carbon atoms. There are in total four valence electrons available for each carbon atom. Three of them are involved in strong covalent  $\sigma$ -bonds with adjacent carbon atoms, giving in-plane stability to the lattice. The last valence electron, along with contributions from other carbon atoms, form an aromatic  $\pi$ -bond which spans the entirety of graphene. These delocalized electrons form the valence and conduction bands in graphene.

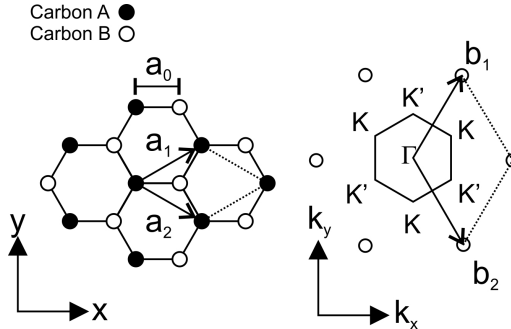


Figure 2.4: **Left:** Real space graphene crystal lattice, which consists of two overlapping triangular sublattices A and B. Black carbon atoms belong to A and white belong to B.  $a_0$  is the distance between adjacent carbon atoms.  $\mathbf{a}_1$  and  $\mathbf{a}_2$  are the lattice vectors, which together with the dotted line span the primitive cell. It contains two carbon atoms in total, one from each sublattice. **Right:** Graphene in reciprocal space with reciprocal lattice vectors  $\mathbf{b}_1$  and  $\mathbf{b}_2$ . The 1st Brillouin zone is hexagonal, with six points,  $\mathbf{K}$  and  $\mathbf{K}'$ , at its corners. The  $\Gamma$  points sits in the center of the BZ.

The reciprocal lattice vectors  $\mathbf{b}_1$  and  $\mathbf{b}_2$  spanning the 1st Brillouin zone (BZ) can be found using the relationship  $\mathbf{b}_i \cdot \mathbf{a}_j = 2\pi\delta_{ij}$ , where  $\delta_{ij}$  is the Kronecker delta. In the corner of the BZ there exist six points, but only two nonequivalent points, called  $\mathbf{K}$  and  $\mathbf{K}'$ , due to sublattice A and B. These six points are also called Dirac points, a reason which will

be apparent later. Using the real space lattice vectors the different reciprocal vectors can be calculated:

$$\begin{aligned}\mathbf{b}_1 &= \frac{2\pi}{3a_0}\hat{\mathbf{x}} + \frac{2\pi}{\sqrt{3}a_0}\hat{\mathbf{y}} \\ \mathbf{b}_2 &= \frac{2\pi}{3a_0}\hat{\mathbf{x}} - \frac{2\pi}{\sqrt{3}a_0}\hat{\mathbf{y}} \\ \mathbf{K} &= \frac{2\pi}{3a_0}\hat{\mathbf{x}} + \frac{2\pi}{\sqrt{3}3a_0}\hat{\mathbf{y}} \\ \mathbf{K}' &= \frac{2\pi}{3a_0}\hat{\mathbf{x}} - \frac{2\pi}{\sqrt{3}3a_0}\hat{\mathbf{y}}\end{aligned}\tag{2.17}$$

The electronic band structure of this relatively simple system can be solved by using a tight-binding approach, where only interactions between nearest-neighbor carbon atoms are taken into account. Assuming that the electrons are tightly bound to their nuclei, the wave functions are given as a linear combination of atomic orbital functions. The tight-binding wave function for the two-atom unit cell of graphene can be expressed:

$$\Psi_{\mathbf{k}}^{\lambda}(\mathbf{r}) = C_{\mathbf{k},A}^{\lambda}(\mathbf{r})\Phi_{\mathbf{k},A}^{\lambda}(\mathbf{r}) + C_{\mathbf{k},B}^{\lambda}(\mathbf{r})\Phi_{\mathbf{k},B}^{\lambda}(\mathbf{r})\tag{2.18}$$

where A, B denote the two atoms in the unit cell,  $\mathbf{k}$  is the electron momentum,  $\lambda$  is the band index, and  $\Phi_{\lambda\mathbf{k}}(\mathbf{r}) = \frac{1}{\sqrt{N}} \sum_{\mathbf{R}_N} e^{i\mathbf{k}\mathbf{R}_N} \phi_{\lambda}(\mathbf{r} - \mathbf{R}_i)$  is the tight-binding wave function with  $\phi_{\lambda}(\mathbf{r} - \mathbf{R}_i)$  being  $2p_z$ -orbital wave functions. The solution to the Schrodinger equation  $H\Psi_{\mathbf{k}}^{\lambda} = E_{\mathbf{k}}^{\lambda}\Psi_{\lambda\mathbf{k}}$  is obtained by multiplying with  $\Phi_{\mathbf{k},A}^{\lambda*}$  and integrating over all space, and then the same for  $\Phi_{\mathbf{k},B}^{\lambda*}$ . The resulting two equations can be written as the matrix equation:

$$\begin{pmatrix} H_{AA} - E_{\mathbf{k}}^{\lambda}S_{AA} & H_{AB} - E_{\mathbf{k}}^{\lambda}S_{AB} \\ H_{BA} - E_{\mathbf{k}}^{\lambda}S_{BA} & H_{AA} - E_{\mathbf{k}}^{\lambda}S_{AA} \end{pmatrix} \begin{pmatrix} C_{\mathbf{k},A}^{\lambda} \\ C_{\mathbf{k},B}^{\lambda} \end{pmatrix} = \begin{pmatrix} 0 \\ 0 \end{pmatrix}\tag{2.19}$$

Where  $H_{ij} = \int \Phi_{\mathbf{k},i}^{\lambda*} H \Phi_{\mathbf{k},j}^{\lambda} d\mathbf{r}$  and  $S_{ij} = \int \Phi_{\mathbf{k},i}^{\lambda*} \Phi_{\mathbf{k},j}^{\lambda} d\mathbf{r}$ . The equivalency of A,B atoms lead to  $S_{AB} = S_{BA}^*$ ,  $H_{AA} = H_{BB}$ ,  $H_{AB} = H_{BA}^*$ . To resolve the transfer matrix element  $H_{AB}$  and overlap integrals  $S_{AB}$  the nearest-neighbor approximation is applied:

$$\begin{aligned}H_{AB} &= \frac{1}{N} \sum_A^N \sum_B^N e^{i\mathbf{k}(\mathbf{R}_B - \mathbf{R}_A)} \langle \phi(\mathbf{r} - \mathbf{R}_A) | H | \phi(\mathbf{r} - \mathbf{R}_B) \rangle = \\ &= \frac{1}{N} \sum_A^N \sum_{B_{nn}}^3 e^{i\mathbf{k}(\mathbf{R}_B - \mathbf{R}_A)} \langle \phi(\mathbf{r} - \mathbf{R}_A) | H | \phi(\mathbf{r} - \mathbf{R}_B) \rangle = \\ &= \frac{1}{N} N \sum_{\delta_i}^3 e^{i\mathbf{k}\delta_i} \langle \phi(\mathbf{r} - \mathbf{R}_A) | H | \phi(\mathbf{r} - \mathbf{R}_A - \delta_i) \rangle = \\ &= \gamma_0(e^{i\mathbf{k}\delta_1} + e^{i\mathbf{k}\delta_2} + e^{i\mathbf{k}\delta_3})\end{aligned}\tag{2.20}$$

$\delta_i$  are the vectors to the three nearest carbon atoms and are in terms of graphene lattice vectors  $\delta_1 = \frac{1}{3}(a_1 + a_2)$ ,  $\delta_2 = \frac{1}{3}(a_2 - 2a_1)$  and  $\delta_3 = \frac{1}{3}(a_1 - 2a_2)$ . This results in (analogous

for  $S_{AB}$ ):

$$\begin{aligned} H_{AB} &= \gamma_0 e^{i\frac{1}{3}\mathbf{k}(\mathbf{a}_1+\mathbf{a}_2)}(1 + e^{-i\mathbf{k}\mathbf{a}_1} + e^{-i\mathbf{k}\mathbf{a}_2}) = \\ &= \gamma_0 e^{i\frac{1}{3}\mathbf{k}(\mathbf{a}_1+\mathbf{a}_2)} f(\mathbf{k}) \\ S_{AB} &= s_0 e^{i\frac{1}{3}\mathbf{k}(\mathbf{a}_1+\mathbf{a}_2)} f(\mathbf{k}) \end{aligned} \quad (2.21)$$

$\gamma_0$  and  $s_0$  are real-valued and correspond to hopping integral and orbital overlap integral respectively.

To find the energy eigenvalues  $E_{\mathbf{k}}^{\lambda}$  of graphene one has to calculate the determinant of equation 2.19. Before solving the aforementioned equations, some matrix elements can be set.  $H_{AA} = H_{BB} = \epsilon_0$  is the self/site energy of the atomic orbitals.  $S_{AA} = S_{BB} = 1$  because the atomic orbital wave functions are normalized. The determinant now can be expanded and solved to yield an expression for the band structure of graphene (dropping the band index):

$$E_{\mathbf{k}} = \frac{\epsilon_0 \pm \gamma_0 |f(\mathbf{k})|}{1 \pm s_0 |f(\mathbf{k})|} \quad (2.22)$$

As expressed above  $f(\mathbf{k}) = (1 + e^{-i\mathbf{k}\mathbf{a}_1} + e^{-i\mathbf{k}\mathbf{a}_2})$  and  $|f(\mathbf{k})| = ((1 + e^{-i\mathbf{k}\mathbf{a}_1} + e^{-i\mathbf{k}\mathbf{a}_2})(1 + e^{i\mathbf{k}\mathbf{a}_1} + e^{i\mathbf{k}\mathbf{a}_2}))^{\frac{1}{2}}$  which in its simplified form is:

$$|f(\mathbf{k})| = \sqrt{3 + 2 \cos(\mathbf{k}\mathbf{a}_1) + 2 \cos(\mathbf{k}\mathbf{a}_2) + 2 \cos(\mathbf{k}\mathbf{a}_1 - \mathbf{k}\mathbf{a}_2)}. \quad (2.23)$$

The three tight-binding parameters  $\epsilon_0$ ,  $\gamma_0$  and  $s_0$  can be determined by for instance experimentally measuring the Fermi velocity, or from ab initio considerations. For strictly nearest-neighbor interactions it is common to set  $\epsilon_0 = 0$ , and this results in the valence and conduction bands crossing at the K point as observed in experiments. The hopping energy is usually set to  $\gamma_0 \approx -3$  eV [31]. The overlap integral  $s_0$  governs the asymmetry between conduction and valence bands as is only relevant at higher energies. Close to zero energy, where conduction and valence band meet, this effect can be safely neglected  $s_0 = 0$ . The low-energy band structure for graphene, plotted in Figure 2.5, is then:

$$\begin{aligned} E_{\mathbf{k}} &= \pm \gamma_0 |f(\mathbf{k})| = \sqrt{3 + 2 \cos(\mathbf{k}\mathbf{a}_1) + 2 \cos(\mathbf{k}\mathbf{a}_2) + 2 \cos(\mathbf{k}\mathbf{a}_1 - \mathbf{k}\mathbf{a}_2)} = \\ &\pm \gamma_0 \sqrt{3 + 2 \cos(\sqrt{3}a_0 k_y) + 4 \cos(\frac{3a_0}{2}k_x) \cos(\frac{\sqrt{3}a_0}{2}k_y)} \end{aligned} \quad (2.24)$$

$k_x$  and  $k_y$  are the  $\hat{\mathbf{x}}$  and  $\hat{\mathbf{y}}$  components of the wave vector respectively. It is easy to verify that the energy is zero only at  $\mathbf{K}$  or  $\mathbf{K}'$ .

Equation 2.24 can be further simplified by Taylor expansion around the  $\mathbf{K}$  points by using  $\mathbf{k} = \mathbf{K} + \mathbf{q}$  with  $|\mathbf{q}| \ll |\mathbf{K}|$  and ignoring higher order terms  $\mathcal{O} = \mathbf{q}^2/\mathbf{K}^2$ . This leads to the linear dispersion:

$$E_{\mathbf{k}} = \hbar v_F |\mathbf{q}| \quad (2.25)$$

$v_F$  is the Fermi velocity  $v_F = 3\gamma_0 a_0/2$  which is on the order of  $v_f \approx 10^6$  m/s. The linear dispersion close to the  $\mathbf{K}$  points is reminiscent of ultra-relativistic particles with

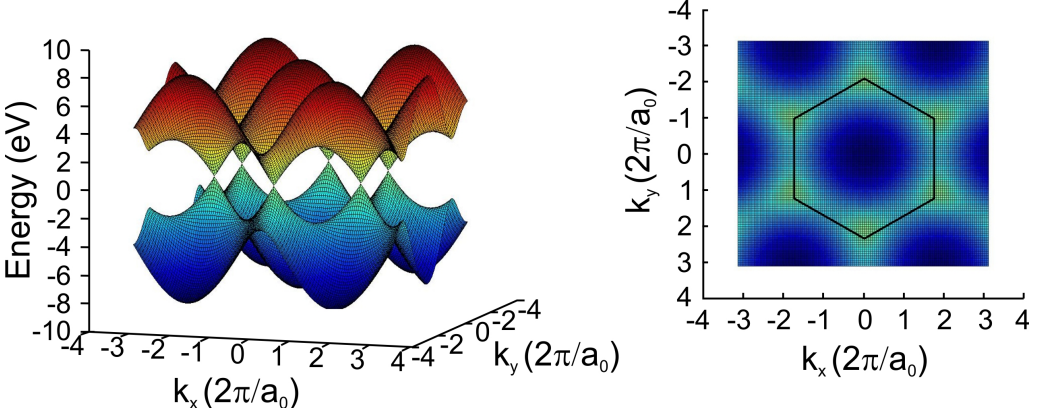


Figure 2.5: **Left:** Band structure of graphene calculated using the nearest-neighbor tight-binding model, with tight-binding parameters set to  $\epsilon_0 = s_0 = 0$  and  $\gamma_0 = -3$  eV. The valence and conduction band meet at six Dirac points in the reciprocal space. The dispersion is linear close to the Dirac points at low energy,  $|E| < 3$  eV. **Right:** Top-down view of the band structure. The six Dirac points exist at zero energy (yellow/green color) and mark the corners of the 1st BZ.

zero rest mass like photons. Consider the energy momentum relation  $E^2 = |\mathbf{p}|^2 c^2 + m^2 c^4$  which for massless particles reduces to  $E = c |\mathbf{p}| = \hbar c |\mathbf{k}|$ . This expression is identical to that of graphene, in fact  $v_f \approx c/300$ . For such particles, the Schrödinger equation reduces to the 2D Dirac equation which is used to describe the behavior of massless Dirac fermions. It is for this reason that the  $\mathbf{K}$  points are called Dirac points.

The linear dispersion creates a conical shape, a Dirac cone, in reciprocal space. The density of states can then be calculated by considering the states living on an annulus with radius  $k$  and thickness  $dk$  in reciprocal space, divided by the area of one state. The area of the annulus is  $2\pi k dk$  and the area of one state is  $(2\pi/L)^2$  where  $L$  is some unit length. Factoring in spin and valley (one dirac cone for  $\mathbf{K}$  and  $\mathbf{K}'$ ) degeneracy, the number of states is  $N = 2k dk L^2 / \pi$ . From the linear dispersion  $dE/dk = \pm \hbar v_F$  and  $dk = |E| dE (\hbar v_F)^2$ . The density of states (DOS), per unit area  $L^2$ , for graphene is:

$$DOS(E) = \frac{2|E|}{\pi(\hbar v_F)^2} \quad (2.26)$$

The density of states is linear with energy and vanishes at the Dirac point. In theory this means that, at zero temperatures, graphene is insulating at the Dirac point with infinite resistance. Since there is no band gap, graphene is referred to as a zero band gap semimetal. In practice, there are other factors such as spatial charge disorder which complicate this picture. Experiments at the Dirac point show finite resistance, with the maximum resistance of graphene being some what controversial with different theories predicting different values [32].

From the expression of DOS an expression for the Fermi energy can be derived.

Consider the charge carrier density  $n$  (number of carriers per area) above zero energy:

$$n = \int_0^\infty DOS(E)f(E)dE \quad (2.27)$$

At zero temperature the Fermi distribution turns into the Heaviside step function ( $=1$  for energies below  $E_F$ , zero otherwise) and the upper energy limit becomes the Fermi energy  $E_F$ . The integration becomes trivial and the charge carrier density is:

$$n = \frac{E_F^2}{\pi(\hbar v_F)^2} \quad (2.28)$$

The Fermi energy depends on the square root of charge carrier density:

$$E_F = \hbar v_F \sqrt{\pi n} \quad (2.29)$$

## 2.2.2 Two Band Hall Effect

Equations 2.9 and 2.10 in Section 2.1.1 reveal how one can extract the charge carrier density and mobility from Hall measurements. They are however only exact in the case of one type of charge carrier, either electrons or holes (single band). As mentioned above, graphene is a zero band gap semimetal and this complicates the picture. The absence of forbidden states enable continuous tuning from p-type carrier to n-type carrier, using for instance an electrostatic gate [11]. This behavior is called ambipolar transport, and is well-known for field-effect transistors in the semiconductor industry.

In the limit of highly doped graphene, the large Fermi energy acts as a barrier suppressing the excitation of minority carriers and the situation is the same of for single band. What constitutes highly doped graphene is in this case dependent on the temperature. As an example, for relatively low doping of  $n = 10^{10} \text{ cm}^{-2}$  the Fermi energy of graphene is 12 meV. The thermal energy at cryogenic temperatures of 2 K is only 0.2 meV. The Fermi-Dirac distribution says that the probability of finding an occupied state at 1 meV above the Fermi energy is < 1%.

In the case when graphene is very close to charge neutrality both holes and electrons can contribute to electrical transport, and this is the ambipolar regime. Ambipolar transport can occur either because of thermal excitation, which is present for any finite temperature due to zero band gap, or the presence of spatial charge disorder which creates regions of p-doping and n-doping (charge puddle regime) [33].

By taking into account both electrons and holes the low-field Hall coefficient becomes:

$$R_H = -\frac{1}{e} \frac{n_e \mu_e^2 - n_h \mu_h^2}{e(n_e \mu_e + n_h \mu_h)^2} \quad (2.30)$$

Where  $n_e, \mu_e$  and  $n_h, \mu_h$  denote electrons and holes respectively. The effective charge carrier density is:

$$n_{eff} = \frac{e(n_e \mu_e + n_h \mu_h)^2}{n_e \mu_e^2 - n_h \mu_h^2} \quad (2.31)$$

The longitudinal sheet resistance  $\rho_{XX}$  is:

$$\rho_{XX} = \frac{1}{e(n_e\mu_e + n_h\mu_h)} \quad (2.32)$$

Exactly at charge neutrality, when the Fermi energy is zero, but at finite temperatures the number of excited electron and holes carriers is identical  $n_e = n_h > 0$ . The effective charge carrier density can be reduced to  $n_{eff} = \alpha n_e$  with the coefficient dependent on the mobility ratio  $\alpha = (\frac{u_e}{u_h} + 1)/(\frac{u_e}{u_h} - 1)$ . For electron-like behavior  $\alpha > 0$  and vice versa for hole-like behavior  $\alpha < 0$ .

Taking into account both thermal excitations and spatial charge disorder (Gaussian probability distribution with disorder strength characterized by  $s$  [34]) the charge carrier density for charge neutral graphene can be expressed as [32]:

$$n_e(T) = n_h(T) = \frac{2}{\pi(\hbar v_F)^2} \left[ \frac{s^2}{4} + \frac{(\pi k_B T)^2}{12} \right] \quad (2.33)$$

Here it is assumed that the disorder strength  $s$  and mobility ratio  $\alpha$  are constant in the considered range of temperatures.

### 2.2.3 Half-integer Quantum Hall Effect

As seen above the physics of graphene near the Dirac points is governed by Dirac equations and is anomalous in the sense of effectively massless fermions. Additionally, due to the A and B sublattices, the Dirac Fermions posses a pseudo-spin and accrue a geometric (Berry) phase of  $\pi$  when completing one orbit, changing the sign of the wave function [35]. This impacts the physics behind the cyclotron motion of graphene carriers in a magnetic field [12]. The cyclotron orbit is changed to:

$$\omega_c = \sqrt{2} \frac{v_F}{l_B} = v_F \frac{2eB}{\hbar} \quad (2.34)$$

Solving the Dirac equation in the presence of a magnetic field yields the LL spectrum of graphene:

$$E = \pm \hbar \omega_c \sqrt{N} = v_F \sqrt{2\hbar eBN}, N = 0, 1, 2... \quad (2.35)$$

The LL of graphene differ from that of conventional 2D systems in three significant ways. Firstly, the energy spacing is no longer equidistant and scales as  $\Delta E \propto \sqrt{B}$  instead of linearly with magnetic field. Secondly, the degeneracy of each LL is increased by an additional factor of 2, owing to the valley degeneracy ( $\mathbf{K}$  and  $\mathbf{K}'$ ). Lastly, there exist a LL even at zero energy which is shared by the two valleys (thus only spin degenerate). These facts significantly affect the behavior of the plateaus in  $R_{XY}$ . Recall that the number of electrons (per unit area) required to fill a single LL in the case of conventional 2D systems is  $B/\Phi_0$ . Now including spin and valley degeneracy each filled LL in graphene contributes  $4B/\Phi_0$  electrons, except the zero energy LL which only contributes  $2B/\Phi_0$ . For  $N$  completely filled LLs above zero energy ( $N = 0$  means that only the zero energy LL is filled) the charge carrier density for graphene is:

$$n = N \frac{4eB}{\hbar} + \frac{2eB}{\hbar} = \frac{4eB}{\hbar} (N + 1/2) \quad (2.36)$$

Inserting the expression for charge carrier density into the equation for the Hall effect:

$$R_{XY} = \frac{B}{en} = \frac{h}{4e^2(N + 1/2)} \quad (2.37)$$

Instead of having plateaus at integer multiples of  $h/e^2$ , the quantized values for graphene are half-integer multiples of  $h/4e^2$ . Compared to conventional filling factors for  $h/\nu e^2$ ,  $N = 1, 2, 3, 4, \dots$ , graphene instead has the progression  $\nu = 2, 6, 10, 14, \dots$

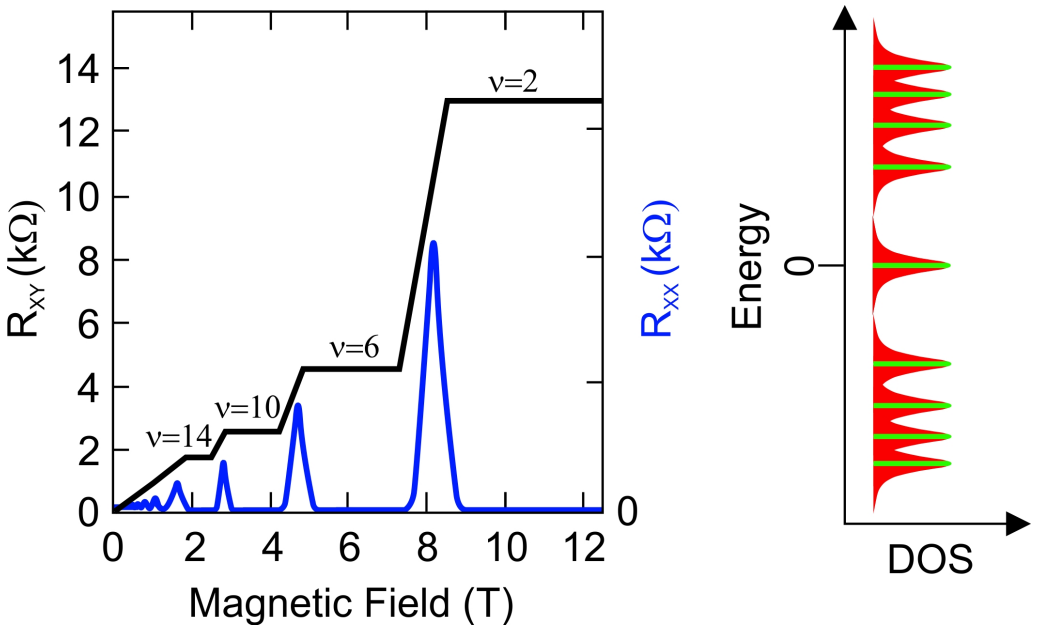


Figure 2.6: **Right:** Schematic representation of the evolution of transverse resistance  $R_{XY}$  and longitudinal resistance  $R_{XX}$  for graphene as one increases magnetic field. The unique progression of  $R_{XY}$  plateaus, compared to conventional 2DEGs, is a fingerprint of monolayer graphene and its Dirac nature. **Left:** LL spectrum for graphene. Note the large energy spacing between the 1st and 0th LL, and the inequidistant energy spacing between LLs.

The unique LL energy spacing of graphene has positive benefits for practical applications. The energy spacing between the zero energy LL and first LL is particularly large in graphene. It means that QHE with  $\nu = 2$  and  $R_{XY} = h/2e^2$  can be observed at lower fields and/or higher temperatures than in conventional systems such as GaAs based 2DEGs. For instance at a magnetic field of 1 T, the energy spacing between the 0th and 1st LL in graphene is over 20 times larger than the LL energy spacing in GaAs 2DEGs. This large energy spacing has allowed for the observation QHE in graphene at room temperatures [36].

## 2.2.4 Epitaxial Graphene on Silicon Carbide

Graphene grown on silicon carbide is greatly influenced by coupling to the substrate. For QHE the relevant effect come from interactions with the substrate and an interface layer, which affect the electronic properties of SiC/G. Section 3.1 will discuss the practicalities of the growth process itself.

SiC is a crystal which consists of Si and C atoms. The structure of a SiC crystal can be thought of as consisting of layers of tetrahedrally bonded Si-C atoms pairs. There are many polytypes of SiC but the common ones used for growth of graphene are the hexagonal polytypes 4H-SiC and 6H-SiC. The number describes the number of Si-C pairs stacked in a unit cell, and H indicates their hexagonal crystal structure. Due to stacking faults of the hexagonal polytypes there is a spontaneous polarization which can introduce p-doping in quasi-freestanding graphene [37]. The polar SiC has two types of surface termination: Si atoms (Si-face) or C atoms (C-face). Monolayer graphene is typically grown on the Si-face, due to slower and more controlled growth process [19]. The growth on the C-face results in multi-layered patchy graphene [38]. Growth on the Si-face is therefore exclusively used for applications which demand high electronic quality graphene, like for QHR standards reliant on the QHE.

Growth of SiC/G proceeds by thermal decomposition of the SiC substrate. At sufficiently high temperatures Si-atoms sublime and leave behind a carbon rich layer which eventually forms graphene. However, the first layer which forms is insulating due to roughly 30% of the carbon atoms forming covalent bonds to the SiC substrate and thus destroying the  $\pi$  bands. This layer is therefore referred to as buffer or interface layer. The second layer forms the actual conducting monolayer of graphene, with its electronic properties mostly intact. Because of their proximity ( $< 4 \text{ \AA}$ ) the graphene layer is influenced by the buffer layer. The buffer layers acts as a donor and gives rise to high intrinsic n-doping of SiC/G, which is on the order of  $n \approx 10^{13} \text{ cm}^{-2}$ . Additionally, the buffer layer has a high density of states and effectively pins the Fermi level of SiC/G, reducing the gate efficiency when trying to tune the charge carrier density of SiC/G [20]. This reduction can decrease the gate capacitance by over 90%. The silicon carbide substrate also plays a role in the aforementioned effects due to unsatisfied dangling bonds on the surface [37]. For practical applications of QHE it is desirable to combat the influence of the buffer layer in order to bring SiC/G close to neutrality so that QHE is observable at low magnetic fields ( $< 5 \text{ T}$ ,  $4 \text{ K}$ ) [17].

While the charge transfer between graphene and the buffer layer makes it difficult to bring SiC/G close to charge neutrality, there is a positive side-effect on the robustness of the quantum Hall plateau. This charge transfer process leads to a magnetic field dependent charge carrier density, which has the effect of greatly prolonging the  $R_{XY} = h/2e^2$  plateau, with experiments showing the plateau up to 50 T [18].



# 3 Experimental Methods

The road from basic materials to a finished, working, electronic graphene device is often long and arduous. This chapter describes in detail the fabrication and characterization processes for SiC/G devices, and how they become functional QHR standards. The first section focuses on the growth of SiC/G through thermal decomposition of SiC. Additionally, this section also presents non-invasive methods such as atomic force microscopy (AFM), optical microscopy, and Raman spectroscopy, which are useful when assessing the quality of the grown material. The second section is entirely about microfabrication, and discusses how one goes from a sheet of graphene to an electronic device using lithographic techniques. The third section presents how graphene can be chemically doped using F4TCNQ and how the mechanism of the F4TCNQ doping technique can be analyzed using secondary ion mass spectroscopy (SIMS) and grazing incidence wide-angle x-ray scattering (GIWAXs). The final section discusses electrical measurement techniques, such as Hall measurements, which are useful when characterizing the performance and quality of a graphene devices, and integral in order to understand the effect of chemical doping.

## 3.1 Graphene Growth

There exists many methods to grow graphene, each with its strengths and weaknesses. Depending on the method, the size of monocrystalline domains and disorder in the material can vary significantly. Some of the current approaches to growth of high (electronic) quality graphene include: mechanical exfoliation, chemical vapor deposition (CVD), and epitaxial growth. Mechanical exfoliation produces the highest-quality material, but the throughput is low and the process is not scalable due to manual operation. CVD utilizes a carbon-rich precursor gas and a metallic catalyst substrate to grow graphene. This technology is scalable and the material quality can be high, however transfer of graphene to an insulating substrate is required for device fabrication. This is a process which introduces additional complications such as contamination and degradation of graphene. Epitaxial growth of graphene utilizes thermal decomposition of a SiC substrate. This method produces a monocrystalline graphene over an entire wafer [19], and is advantageous for device fabrication since SiC can be insulating at room temperature. All work in this thesis has been done using SiC/G grown on the hexagonal SiC polytype 4H-SiC. An outline of the growth process is given below, for exact recipes consult Appendix A.

The starting point is the SiC substrate itself. Growth of SiC/G has historically been performed on either hexagonal polytypes 6H-SiC or 4H-SiC. These substrates are insulating ( $\approx 3$  eV bandgap), have a crystal structure commensurate with the graphene lattice, and, most importantly, readily available in industry where high quality, large areas wafers, are sold at a moderate price. It is important that the substrate is clean and free from defects since any imperfection will nucleate growth, leading to inhomogeneous graphene. Aside from buying the highest grade SiC possible, the substrates are thoroughly cleaned before the growth process. In the first fabrication step the wafers are diced into 7 mm x 7 mm square chips. These chips then undergo the RCA process (See A.1), an industry standard in the semiconductor business, where organics contaminants are

removed using ammonia water mixed with hydrogen peroxide, oxides are removed using hydrofluoric acid (HF), and metallic contaminants are removed using hydrochloric acid mixed with hydrogen peroxide. After the RCA process the chips are carefully, and repeatedly, rinsed in a bath of high-purity water. Immediately before the growth step, the chips are dipped one final time in HF acid and quickly transferred, submerged in water, to the growth oven. In the center of the oven there is a crucible of solid graphite, on top of which the chip rests, suspended on graphite pillars. The crucible is enclosed in a quartz tube, whose outside is surrounded by a coil and water cooling system. When aiming to grow monolayer graphene the oven is heated to approximately 1700 °C using a RF-generator, and the chamber is filled with an inert argon atmosphere of 800 mbar. The oven is kept at this temperature for 5 minutes, after which the power is turned off and the system is left to slowly cool down over 4 hours. After the sample is sufficiently cold it is removed from the oven and inspected using non-invasive techniques to determine the quality, and area coverage, of monolayer graphene.

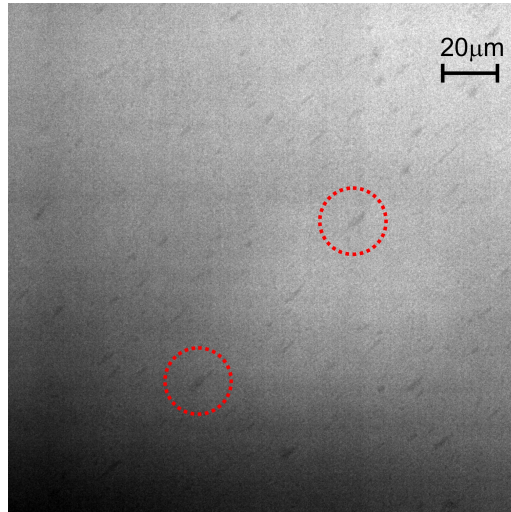


Figure 3.1: An image of SiC/G taken using transmission mode optical microscopy. Digital contrast enhancement such as gamma correction has been used to better image the bilayer inclusions. Bilayer inclusion absorb more of the transmitted light and appear as dark stripes (examples given inside red dotted circles). Everywhere else is monolayer graphene and the area coverage of this particular area is estimated to be > 98%. Note that the presence of monolayer is in principle not verifiable from this optical image alone, it simply serves as a hint whether a particular sample is worthy of further processing or not.

### 3.1.1 Optical Microscopy

Despite the fact that both the SiC substrate and graphene are mostly transparent, optical microscopy techniques can still yield valuable information on the homogeneity of growth [39]. Using transmission mode microscopy, and digital contrast enhancement if needed, one

can distinguish between single and multi-layer graphene patches because each additional layer of graphene absorbs an additional  $\approx 1.3\%$  of the transmitted light. The advantage of this method is that it allows for quickly assessment of the quality of a SiC/G chip over a large area and in real-time. An example of an image produced using this technique can be seen in Figure 3.1. In general this method can only give a relative measure, i.e. how many extra layers of graphene is in one region compared to another. To determine the absolute layer number a known reference, such as bare SiC, is needed.

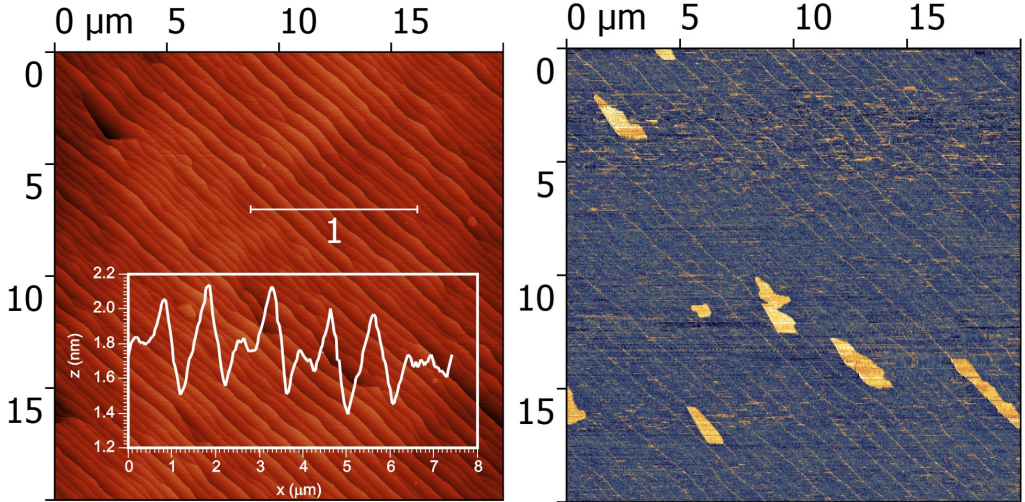


Figure 3.2: SiC/G characterized by tapping mode AFM. **Left:** Height image showing the topography of SiC/G (note that a linear background has been subtracted). In height the most prominent feature is the steps formed on the surface of the SiC substrate during growth. The inset shows the height profile taken along Line 1, revealing that the steps are on the order of 1 nm hight, and separated by atomically flat terraces 1-2  $\mu\text{m}$  wide. The graphene itself is draped like a carpet over this landscape. Certain regions have much higher SiC steps, and appear almost as holes (black). This is a hint of multilayer growth, presumably bilayer if the surrounding is monolayer. **Right:** The phase image clearly reveals the presence of bilayer inclusions (yellow).

### 3.1.2 Atomic Force Microscopy

While optical microscopy is a convenient and quick method to assess the homogeneity of growth, it lacks the ability to resolve features on the nanometer scale. A scanning probe technique such as AFM is useful when lateral resolution below 50 nm is needed. Furthermore, it can provide atomic resolution in height and can be used to image the topography of the sample (Figure 3.2). The common mode of operation is tapping mode AFM, where a sharp tip on an oscillating cantilever, driven near its resonance frequency, is intermittently brought close to the sample. The change in oscillation amplitude due to interactions with the surface can be used to extract information about the height. This

signal is primarily useful for determining the topography, which in the case for SiC/G displays nanometer-sized SiC steps and atomically flat terraces, over which a continuous layer of graphene is draped. Beside the topographical information, the mechanical properties and viscoelasticity on the underlying material can be gleamed from the phase signal, which is simply the phase difference between the excitation signal of the cantilever and the measured output signal. This is a measurement of the energy loss and can be used to distinguish between different graphene domains, but only to the extent that two regions have different graphene thickness. An extension of regular tapping mode AFM is the electrical mode kelvin probe microscopy (KPM) which can be used to image the work function of the underlying material. With a known reference point, such as gold, one can determine the work function of the underlying material [40] and in principle (if the number of layers is known) estimate the charge carrier density.

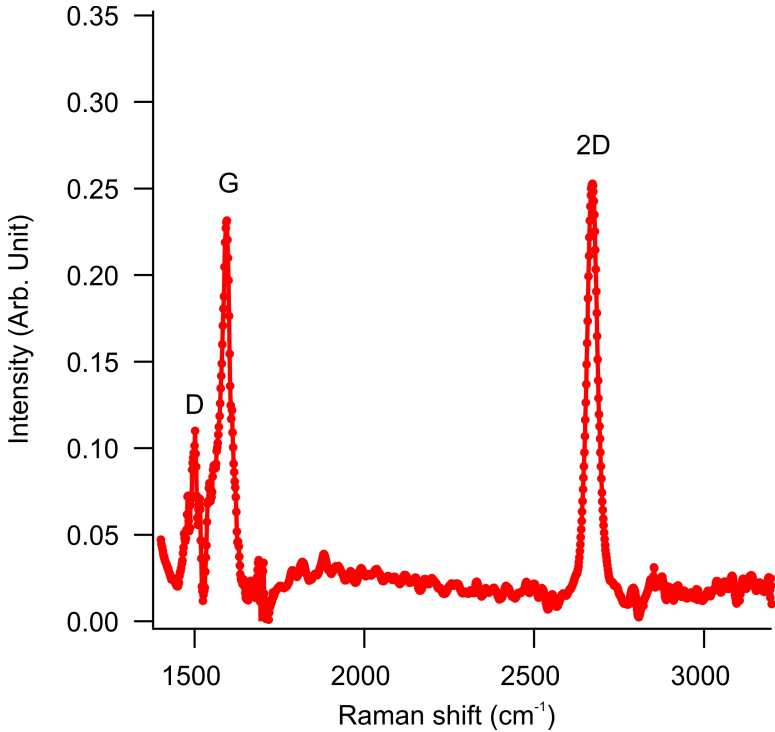


Figure 3.3: Raman spectra of SiC/G, with the SiC background subtracted. A clear 2D peak can be seen at  $2670\text{ cm}^{-1}$ . The D ( $1500\text{ cm}^{-1}$ ) and G ( $1590\text{ cm}^{-1}$ ) peaks, while slightly distorted due to the subtracted SiC signal, are also clearly visible. The sharp (FWHM  $40\text{ cm}^{-1}$ ), single Lorentzian, 2D peak combined with the relatively weak D peak indicate that the quality of SiC/G is good.

### 3.1.3 Raman Spectroscopy

A common technique to characterize graphene is through Raman spectroscopy. This technique relies on inelastic scattering of monochromatic light and probes the vibrational modes of a system, which reveals information about the crystal structure. Graphene has many unique finger prints in a Raman spectra [41], but the main peaks which are interesting are the 2D peak (due to the breathing mode of six carbon atom rings), D peak (same fundamental reason as 2D peak, but activated by disorder) and G peak (in-plane vibrational mode of carbon-carbon bonds). Figure 3.3 shows an example for SiC/G. A sign of high quality monolayer graphene is an intense, sharp, 2D peak with a small D peak. There are other subtleties in the Raman spectra, such that the position, width and intensity of the 2D and G peak depend on strain and doping. Furthermore, additional graphene layers will broaden (in fact superposition of several peaks) and shift the 2D peak [42]. However, due to influences of strain and doping (and limited lateral resolution of regular Raman spectroscopy) it is not always possible to clearly distinguish between mono and multilayer graphene. An unfortunate coincidence of Raman spectroscopy on SiC/G is that SiC has many peaks which overlap with D and G peak of graphene. While careful background subtraction can recover the buried peaks, the unaffected 2D peak remains the most trustworthy.

## 3.2 Microfabrication

In this section we will describe the general lithography process used to pattern graphene into an electronic device. For a full description of the recipes see Appendix A.2. The primary fabrication technique relies on electron beam lithography (EBL) to transfer patterns to SiC/G. Photolithography is a viable alternative, but it is not used in this work. In order to produce a working device a minimum of three EBL steps are needed.

In the first EBL steps (Figure 3.4, step 1) metallic markers (typically cross shaped) are made to enable precise alignment of future layers. In the same process, so-called metallic anchors are also created. These anchors ensure that the eventual metallic contacts connected to graphene adhere well to the chip. It is a crucial and necessary precaution since adhesion between metals, for instance Au, and graphene is poor. The process begins when SiC/G chips, which have passed initial inspection using the aforementioned techniques in Section 3.1, are covered by two layers of EBL compatible resist using spin coating. The bottom layer, closest to graphene, consists of a poly(methyl-methacrylate) (PMMA) based copolymer and the top layer consists of A-RP 6200.13. These are both positive resists, which become soluble in specific developers upon exposure to a beam of electrons. Furthermore, these two resists are sensitive to different developers which enable control over the resist profile. The desired pattern is transferred to the resist through direct writing with an electron beam. After exposure the top layer is developed in o-xylene and the bottom layer is developed using isopropanol (IPA) mixed with water. The respective development times are tuned such that the bottom layer becomes more developed than the top layer, effectively creating an undercut in the resist profile. This facilitates the removal of the resist layers after metal evaporation. After the resist has been developed the underlying graphene is now preferentially exposed, according to the

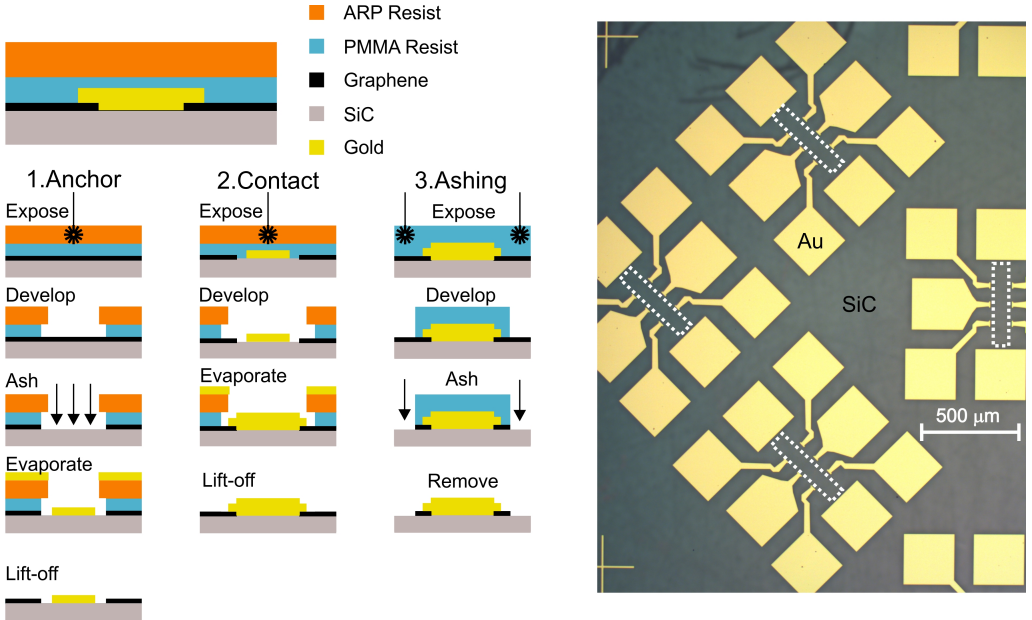


Figure 3.4: Left: Schematic representation of three EBL steps. **1. Anchor:** The 1st EBL step aims to fabricate Au anchors and markers. Graphene is removed using oxygen plasma ashing and the layer is deposited directly on SiC for better adhesion. The markers are used to align future layers, while the anchors provide support and improve adhesion for the eventual electrical contacts connected to graphene. **2. Contact:** The 2nd EBL step uses the markers from the 1st step to align Au contacts to graphene. **3. Ashing:** In the final step the geometry of the Hall bar is defined by removing excess graphene using ashing. This steps also ensures that separate Hall bar devices on the same chip are electrically disconnected from each other. **Right:** Optical image of a finished SiC/G sample, with several Hall bar devices. Each Hall bar device has eight electrical contacts made from Au. The white dotted line mark the rectangular graphene Hall bars. Graphene has been removed from the rest of the chip, leaving behind only insulating SiC.

desired pattern. In order to promote adhesion of the metallic film the graphene is removed using oxygen plasma etching (ashing), revealing the SiC substrate underneath. A thin film of Ti (interface layer) followed by a thin film of Au are evaporated over the entire chip. This is a physical vapor deposition (PVD) process in which the material is evaporated from a crucible using an electron beam. Finally, the remaining resist along with the excess metal are removed using acetone in the lift-off process.

In the second EBL step (Figure 3.4, step 2) metallic contacts are connected to graphene. The procedure is identical to the first EBL step, with the sole exception that the oxygen plasma etching of graphene is omitted since electrical contact between metal and graphene itself is needed. Using the markers made in the first step the metallic contact pads and leads are aligned to the anchor layer. Their placement is designed to contact graphene

in Hall bar geometry. For a typical graphene Hall bar there are eight contacts in total, two for source and drain and six for voltage probes. Each 7 mm x 7 mm chip can house several graphene Hall bar devices.

In the final EBL step (Figure 3.4, step 3) the geometry of the graphene hall bar itself is defined. Up until now the entire chip is still connected by a continuous layer of graphene. In order to electrically isolate the different graphene Hall bar devices from each other, and to ensure that the current takes a well-defined path within each device, graphene needs to be patterned using oxygen plasma. For this EBL step only one resist layer is required and a simple PMMA resist mask is used. Similar to the first EBL step, the sample is exposed to electron beam irradiation, developed using IPA mixed with water and etched using oxygen plasma. The residual resist is removed using acetone.

The dimensions of graphene Hall bars studied in this work are W=5 mm x L=5 mm for macroscopic samples, and W=2-100  $\mu$ m x L=10-300  $\mu$ m for microscopic ones. Before electrical characterization the fabricated devices are typically encapsulated by a polymer layer in order to protect the surface of graphene from unintentional exposure to dust particles, ambient dopants such as water, or other contaminants.

### 3.3 Chemical Doping

As touched upon in the introduction, the control over charge carrier density in SiC/G is challenging. This section will present a method of how graphene can be chemically doped using an acceptor molecule F4TCNQ mixed with a polymer PMMA. Exact recipes, such as a mixing ratios, can be found in Appendix A.3.

The first step requires preparation of the dopant blend itself. A dry powder of F4TCNQ molecules is dissolved in anisole solvent and the resulting solution is then mixed with PMMA resist, whose solvent is also anisole. The standard dopant blend used throughout this thesis consists of 7 wt.% F4TCNQ molecules in PMMA. Before the dopant blend is applied to SiC/G, a polymer layer of neat PMMA or copolymer PMMA is first deposited using spin coating. This layer acts like a spacer layer and affects the diffusion of F4TCNQ dopants, and the doping recipe has been optimized with this spacer layer in mind. The dopant blend is then spin coated directly onto the spacer layer. Lastly, and most importantly, the resist is annealed at elevated temperatures, above the glass transition temperature of PMMA, of 160 °C. This step is common for EBL process to remove residual solvent from the resist. However, the main purpose here is to use the annealing process to tune the final charge carrier density of doped SiC/G. It is observed that continued thermal annealing at these temperatures irreversibly reduces the doping effect of F4TCNQ molecules, causing SiC/G to be more n-doped with increasing annealing time. In fact, using the standard dopant blend, samples can be either p-doped or n-doped depending on annealing time. The optimal annealing time in order to achieve charge neutral graphene is around 5 min, for samples covered by a spacer layer and dopant layer on top,

For more advanced measurement which require tuneable carrier density in real-time, an electrostatic topgate can be deposited directly on top of the polymer layers. This process requires additional layers of spacer PMMA and dopant blend in order to preserve the doping level of the underlying SiC/G. Caution is taken not to affect the dopants by

wet chemistry by forgoing EBL and instead using a shadow mask (made using EBL to pattern through-holes in a thin Si wafer) to evaporate the gate electrode.

### 3.3.1 Secondary-ion Mass Spectroscopy

In order to better understand the mechanism behind F4TCNQ doping of SiC/G secondary-ion mass spectroscopy (SIMS) can be used to provide a chemical profile of the polymer stack, from the top surface all the way down to graphene. More precisely, samples were analyzed using time-of-flight (ToF) SIMS. A primary ion beam sputters away material as it digs further down into the sample. The secondary ions ejected by this process are all accelerated to the same velocity by an external electric field, neglecting small differences in initial velocity, and analyzed by a detector which measures their ToF, and thus obtaining their mass. The high mass resolution of ToF-SIMS allows for the identification of which ions were ejected. Furthermore, SIMS is a surface sensitive technique since particles from the first few monolayers are ejected and the ion intensity is ideally related to surface concentration of a particular species. However, surface roughness and varying sputter rates (different binding energies/material) often lead to broadening of signals.

SIMS samples are prepared with spacer PMMA layer, dopant blend, and one additional encapsulation layer of PMMA. During measurements of chemically doped SiC/G, the unique fingerprints of F4TCNQ are tracked and signals of interest can for instance be fluorine ions (F) and carbon-nitrogen (CN) ions. The signal from silicon (Si) ions serves as a marker for when the SiC substrate has been reached. In practice a gentler pulsed primary ion beam ( $\text{Bi}^{3+}$ , 0.34 pA at 50 keV) is used during the ToF analysis, to prevent excessive surface damage. The sputtering step is performed using a powerful  $\text{C}_60^{++}$  beam at 20 keV with a current of 0.2 nA. The two beams alternate, with 1 second of analysis, followed by 1 seconds of sputtering, and finally 1 second of pause before restarting the cycle.

### 3.3.2 Grazing-incidence Wide-angle X-ray Scattering

Grazing-incidence wide-angle x-ray scattering (GIWAXs) is a powerful technique to investigate the structure of the F4TCNQ molecules inside the PMMA matrix. Like traditional x-ray diffraction, this technique relies on Bragg's law of reflection to determine the spacing between atomic planes. Grazing-incidence refers to the shallow incident angle, suitable for probing thin films due to efficient reflection off of the surface. The wide-angle refers to the collection of wide-angle scattering, which corresponds to a large momentum transfer in the reciprocal space and thus small distances, on the order of nanometers. Imaging thin films, which have comparatively little material as opposed to bulk samples, means that the reflected signal is weak. For all practical purposes the measurements are performed using powerful radiation from a synchrotron source. GIWAXs data were obtained at the D1-beam line at the Cornell High Energy Synchrotron Source (CHESS) at Cornell University.

Chemically doped graphene, prepared with spacer PMMA layer and dopant blend, were investigated using GIWAXs at room temperature and under ambient conditions. A positron beam with wavelength 0.1162 nm was used. The standard incident angle was

0.15 degrees with alternate angles between 0.1-0.25 degrees. However, the attenuation depth at 0.125 degrees is already 500 nm (the distance at which beam intensity drops to  $1/e$  of original intensity), which is enough to penetrate the entire polymer stack. Due to the high intensity samples were not exposed for more than 20 seconds.

### 3.4 Electrical Characterization

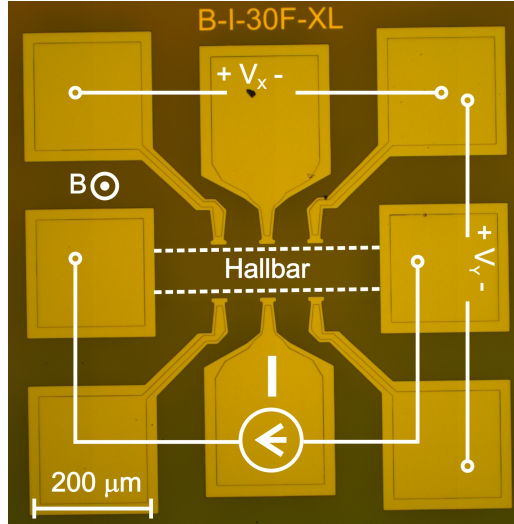


Figure 3.5: Optical image of a SiC/G Hall bar device with eight Au contacts. This device is current biased and subjected to an out-of-plane perpendicular magnetic field  $B$ . The white overlay indicates the current source with current  $I_X$ , the direction of magnetic field  $B$ , and where the longitudinal voltage  $V_X$  and transverse voltage  $V_Y$  are measured. The white dotted lines mark the boundaries of the graphene itself.

The primary electrical characterization tool is Hall and quantum Hall effect (QHE) measurements, which are used to extract important information such as the charge carrier density and carrier mobility. In order to observe quantum transport phenomena, such QHE, samples need to be brought to cryogenic temperatures and subjected to a perpendicular magnetic field. The cooling is achieved by lowering the sample into a gas-flow cryostat in which liquid helium ( ${}^4He$ ) is used. By pumping on the helium samples can be brought to temperatures slightly below  $T=2$  K. The sample temperature is monitored using a diode thermometer mounted within 5 cm of the sample. The cryostat is equipped with a superconducting magnet, capable of high magnetic fields from 9-14 T.

The standard procedure is to current bias the graphene sample and measure voltage in four-probe configuration (Keithley 6221 DC and AC current source, Agilent 34420A nanovolt meter). The current bias is typically in the range of 100 nA, which is a safe range w.r.t. overheating and exceeding the critical current of QHE. Current-voltage

characteristics remain linear in this current range from room temperature down to cryogenic temperatures. Hall measurements are performed by applying a low magnetic field,  $<1$  T, and measuring the transverse Hall resistance (voltage)  $R_{XY}$ . From this the carrier density and carrier mobility can be determined. At cryogenic temperatures it is possible to observe the QHE (depending on magnetic field and doping level). A fully quantized sample, meaning  $R_{XX}=0$  and  $R_{XY}=h/2e^2$ , indicates that the sample is of high electronic quality. All reported values of charge carrier mobility and charge carrier concentration are extracted from four-probe hall/quantum hall measurements. Note that once samples approach the charge neutrality point the hall voltage is no longer linear with magnetic field and those points have been intentionally omitted from carrier density/mobility plots. This indicates when the sample has entered the charge-puddle regime, dominated by charge disorder.

For measurements which require an electrostatic gate the top gate is biased with voltages ranging from -100 to +200 V. The gate voltage is referenced to the sample drain and negative gate voltage induces p-doping while positive voltage induces n-doping. Such high voltages are necessary due to thick dielectric (polymer layers approach 1  $\mu\text{m}$  thickness) and reduced gate efficiency owing to the buffer layer. The measured gate leakage current is kept below  $<1$  nA. It is observed that gate breakdown occurs earlier for negative gate voltages than positive, and this is attributed to the internal electric field due to F4TCNQ molecules.

### 3.4.1 Cryogenic Current Comparator

An eternal struggle in the art of metrology is to decrease the measurement uncertainty. The pinnacle of this can be seen in QHR devices based on SiC/G, which have provided measurements of the resistance quantum  $h/2e^2$  with a precision of 0.86 n $\Omega/\Omega$  (86 parts-per-trillion) [14]. This is no small feat, and it is made possible in part to the cryogenic current comparator (CCC) [43, 44]

The CCC is basically a current comparator bridge where two resistances, called  $R_K$  and  $R_S$ , are compared by placing them in different current loops. Typically  $R_S$  is a sample resistor which is to be calibrated against a QHR standard  $R_K$  with a known value of  $h/2e^2$ . The ratio between the windings  $N_p/N_s$  is adjusted to be as close as possible to the expected resistance ratio  $R_K/R_S$ . The goal is to ensure that the current through both resistors is equal, and measuring the voltage ratio (the detector is often a nanovoltmeter) in order to determine the resistance ratio. The wires which carry the current are fed through a superconducting tube. Thanks to the Meissner effect screening currents form on the inside surface of the tube, exactly canceling the magnetic field inside the superconductor. These screening current flows across the surface of the shield tube, and to the outer surface and induce a magnetic field. This magnetic field is detected by a superconducting quantum interference device (SQUID), which provides the ultimate sensitivity to magnetic flux, with the assistance of a pick-up coil close to the shield. The output signal of the SQUID is then fed back to one of the current sources in order to null the net magnetic field in the CCC shield, which means to accurately adjust the current ratio between the two resistors to match the winding ratio. When the bridge is exactly balanced the reading on the detector is exactly proportional to the resistance ratio. The

detector itself is usually balanced with the use of a third circuit containing a trim coil  $N_t$ , a variable resistor  $R_l$  and a fixed resistor  $R_h$  with high resistance value. With everything in place, the measured resistance ratio is [43]:

$$\begin{aligned} \frac{R_K}{R_S} &= \frac{N_p}{N_s} \frac{1}{1+d} \frac{1}{(1+V_M/V)} \\ d &= \frac{N_t}{N_s} \frac{R_l}{(R_l + R_h)} \end{aligned} \quad (3.1)$$

Where  $V_M$  is the voltage measured by the detector (which should be close to zero) and  $V$  is the voltage across the resistors under investigation. For reference, when comparing the quantum Hall resistance of graphene  $h/2e^2 \approx 12.9064\ldots \text{k}\Omega$  against a  $100 \Omega$  standard resistor the windings are  $N_p = 2065$  and  $N_s = 16$ , with ratio  $N_p/N_s = 129.0625$  which is already very close, but not on the level of  $\text{n}\Omega/\Omega$ .

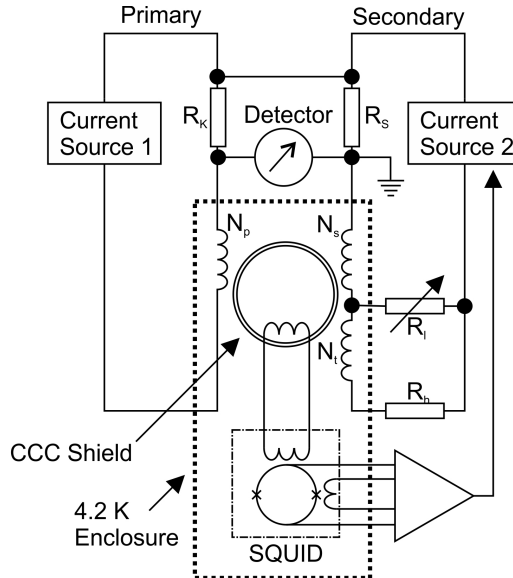


Figure 3.6: Schematic representation of a CCC circuit. The reference resistor  $R_K$ , usually a QHR standard, is compared to another resistor  $R_s$ . The goal is to ensure that the current flowing through both resistors is equal. When balanced the voltage measured by the detector is exactly proportional to the resistance ratio. The ratio between current windings  $N_p/N_s$  is set to be as close as possible to the expected resistance ratio  $R_K/R_s$ . The SQUID ensures that precise balance is kept by measuring the net magnetic field in the superconducting CCC shield and sending the output to one current source as feedback to one of the current sources to null the magnetic field. An additional trim coil  $N_t$ , variable resistor  $R_l$  and high resistance  $R_h$  are used to null the detector itself.



# 4 Results and Discussion

This chapter presents and discusses the experimental results of the thesis. The first section gives a brief overview of work done towards a creating a more user-friendly QHR standard, with the goal of achieving a table-top cryogen-free realization of QHR. At that time SiC/G samples were still fabricated using corona discharge gating, which is not suitable for practical purposes. The second section, and the main findings of this thesis, presents the novel chemical doping method based on F4TCNQ PMMA polymer blend. A detailed description of the effect of F4TCNQ, guided by a polymer matrix, on SiC/G is given, with results from magnetotransport, electrostatic gating, and chemical analysis. The final section shows the initial metrological tests of chemically doped SiC/G QHR standards.

## 4.1 Table-top System

A constant struggle in the field of metrology is to find ways to bring the primary standard closer to the end-user, thereby decreasing the traceability chain. In practice this means that the QHR standard should operate without the need for complicated and bulky laboratory equipment. Ideally, the operation of such a standard should be as simple as pressing a button. Progress toward this goal has been made possible with the advent of QHR based on SiC/G [15], which can operate at higher temperatures, at larger bias currents and lower magnetic fields compared to conventional materials [16, 17].

A table-top cryogen-free QHR cryostat has already been constructed and proved to show quantum Hall measurements with metrological accuracy while operating at 4.2 K and magnetic fields below 5 T [17]. Note that in the first incarnation there is still an externally connected CCC, and more work is required to integrate all components in the same design. Nonetheless, the concept has been successfully demonstrated, with the QHR sample being based SiC/G and fabricated as described in Chapter 3. However, the charge carrier density of the chip was tuned by corona discharge, which is volatile at ambient conditions. This means that every time the system is heated up, re-calibration of the charge carrier density of the QHR standard is required. The repeated tuning of charge carrier density is not only necessary for quantization at 4.2 K and 5 T, but also the optimization of the critical current [17]. This additional layer of complexity is acceptable for research purposes, but not feasible in practice. This prompted the investigation of new, more stable and reliable, methods of controlling the charge carrier density. This endeavor eventually lead to the development of chemical doping using F4TCNQ mixed with PMMA presented below.

## 4.2 Chemical Doping

The p-doping effect of F4TCNQ on SiC/G is well-documented [23, 45]. Previous studies used F4TCNQ directly deposited on SiC/G, and the p-doping effect was observed to increase with thickness, saturating at around one monolayer of F4TCNQ (0.8 nm thick, non-planar adsorption). From photo emission spectroscopy it was found that F4TCNQ has non-planar adsorption and forms a charge-transfer complex with graphene, extracting on average around 0.3-0.5 electrons from graphene. This estimate assumes a doping change of  $\approx 10^{13} \text{ cm}^{-2}$ , monolayer F4TCNQ coverage with 2-4 molecules per  $\text{nm}^2$  (considering size of F4TCNQ [46]) and 10 % gate efficiency of F4TCNQ [20]. However, macroscopic electrical transport properties was complicated by instability at ambient conditions [24]. The approach in this thesis is different, adding PMMA as a host matrix to stabilize the F4TCNQ dopant. The combination yields air-stable, tuneable and reliable doping of SiC/G.

### 4.2.1 Towards charge neutrality

Different doping schemes were tested to explore the possibilities of stable F4TCNQ doping for electrical devices. Figure 4.1 shows three initially tested approaches to chemical doping and their influence the charge carrier density and mobility of SiC/G. Samples were cooled down and magnetotransport measurements were taken at different temperatures to monitor the evolution of carrier density and mobility. The mixture of F4TCNQ acceptor molecules and PMMA polymer (henceforth referred to as dopant blend), combined with a PMMA (or copolymer PMMA) spacer layer, has a strong p-doping effect on SiC/G, capable of bringing SiC/G close to charge neutrality at cryogenic temperatures of 2 K, with charge carrier densities  $n \approx 10^{10} \text{ cm}^{-2}$ . The low doping level leads to a strong temperature dependence of carrier density due to thermal extrication above the Fermi energy, which is only  $\approx 11 \text{ meV}$  at such low doping. The carrier mobility increases correspondingly as temperature decreases, with maximum value reaching  $50,000 \text{ cm}^2/\text{Vs}$ . Note that the downturn in mobility at the lower temperatures is due to the onset of quantum corrections to resistance (weak localization and electron-electron interactions). Pristine SiC/G was achieved through hBN encapsulation of SiC/G and provides a reference point which reveals the intrinsic n-doping of SiC/G to be on the order of  $n \approx 10^{13} \text{ cm}^{-2}$ . Thus, the decrease in charge carrier density compared to the pristine case is three orders of magnitude, similar to the case for direct deposition of neat F4TCNQ. The surface coverage is then comparable to the value from literature, with around 2-4 molecules per  $\text{nm}^2$  or  $2 - 4 \times 10^{14} \text{ cm}^{-2}$ .

Without the spacer PMMA layer, the dopant blend deposited directly on SiC/G acts as a moderate p-dopant. It is also observed that neat PMMA itself acts as a weak p-dopant. However, only in the case when the dopant layer and spacer PMMA layer operate in tandem, was charge neutrality and high carrier mobility obtained. The thickness of the spacer PMMA layer was varied between 100 – 400 nm without any appreciable change in doping. This suggests that there is a minimum spacer layer thickness needed for charge neutral graphene. Therefore, the standard chemical doping technique used in this work to achieve charge neutral SiC/G uses the combination of PMMA spacer and dopant blend,

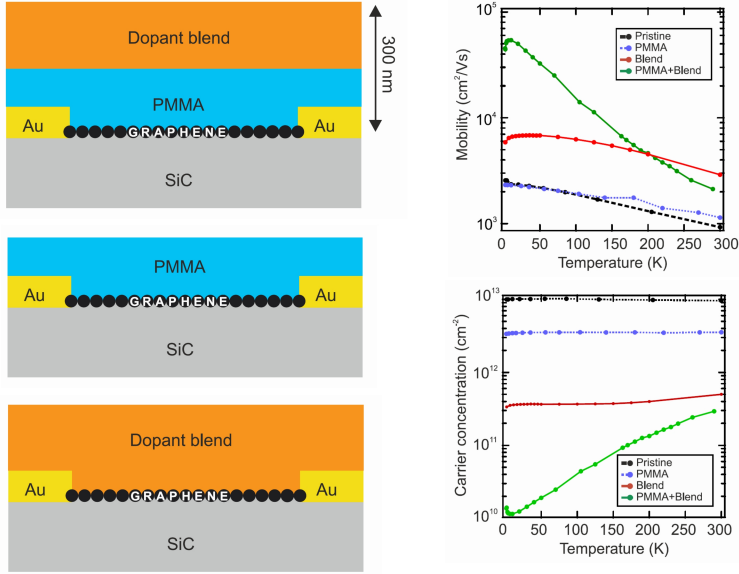


**Figure 4.1:** **Left:** Schematic representation of three chemical doping schemes of SiC/G. The dopant blend consists of F4TCNQ acceptor molecules mixed with PMMA. **Right:** Charge carrier density and mobility extracted from Hall measurements reveal that when the dopant blend and PMMA spacer are used in combination, the charge carrier density of SiC/G decreases by three orders of magnitude compared to pristine SiC/G, reaching a low doping level of  $10^{10} \text{ cm}^{-2}$  at 2 K. The mobility figure is very high, reaching 50,000  $\text{cm}^2/\text{Vs}$  at cryogenic temperatures. The two other tested methods, using only PMMA and only dopant blend, act as weak to moderate p-dopants.

described in Appendix A.3.

Note that for (quantum) Hall measurements performed at cryogenic temperatures the simpler single band Hall model is used to calculate charge carrier density and mobility. Figure 4.2 shows the typical temperature dependence of  $\rho_{XX}$  for SiC/G doped with spacer layer and dopant blend. From 300 K to around 175 K there is a monotonic increase of resistance. This non-metallic behavior is due to the decrease of thermally excited carriers. The maximum of this hump in resistance at high temperatures is closely related to the doping level observed after all of the thermally excited carriers have been frozen. At 175 K the thermal energy scale is  $k_B T \approx 15 \text{ meV}$ . When this energy is well below the Fermi energy of graphene the thermal excitations are suppressed. A Fermi energy of 15 meV corresponds to a charge carrier density of  $n \approx 1.7 \times 10^{10} \text{ cm}^{-2}$ . The quantum Hall measurements performed at 2 K measured the charge carrier density to be  $n \approx 1.5 \times 10^{10} \text{ cm}^{-2}$ , in excellent agreement with the estimate from temperature dependence of resistance. At temperatures below 175 K normal metallic behavior dominates and the resistance decreases linearly with temperature due to suppression of scattering from acoustic phonons. At the Bloch-Gruneisen temperature of around 70 K quantum

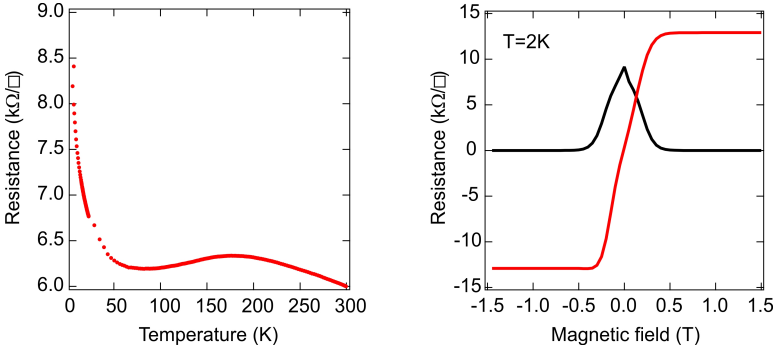


Figure 4.2: **Left:** Temperature dependence of  $\rho_{XX}$  for chemically doped SiC/G as it is cooled down from 300 K to 2 K. The initial increase of resistance is due to the freezing of thermally excited carriers. After passing the hump around 175 K the resistance decreases linearly as is expected for the suppression of phonon scattering. At even lower temperatures quantum corrections to resistance, such as weak localization and electron-electron interactions, give rise to a logarithmic increase of resistance. **Right:** Quantum Hall measurements performed at 2 K. The sample shows QHE below 1.5 T, with  $n \approx 1.5 \times 10^{10} \text{ cm}^{-2}$ .

corrections such as weak localization and electron-electron interactions become apparent and produce a logarithmic temperature dependence [1].

#### 4.2.2 Spontaneous Assembly

In order to gain a better understanding of the F4TCNQ doping process and the role of PMMA, ToF-SIMS was performed. The chemical structure of the F4TCNQ molecule gives rise to unique fingerprints when analyzing the chemical composition of the polymer layers. The two most prominent signs of F4TCNQ came from F ions and CN ions. The Si signal was used as an indicator for when the SiC, and thus graphene, surface was reached. Figure 4.3 shows the SIMS data for a samples prepared with a PMMA spacer layer, dopant blend and an additional PMMA encapsulation layer. Three distinct regions underneath the polymer stack were probed: 1. Graphene surface, 2. Au surface and 3. SiC surface. The measurement probed the spatial distribution of F4TCNQ molecules from the sample surface down to each surface type.

The first measurement was taken of the polymer stack above the surface of graphene. The intense peaks in F and CN signals coincide with the appearance of the Si signal, which is a clear sign of spontaneous accumulation of F4TCNQ molecules near the surface of graphene. The full-width-at-half-maximum (FWHM), in sputter seconds, of the CN peak corresponds to around 10 nm in thickness. However since the spatial resolution of SIMS is limited due to surface roughness and/or uneven sputtering broadening of the peak is to be excepted. Taking the SIMS intensity as an approximation for surface density, the surface coverage of F4TCNQ at near graphene is now over 50 % greater than inside the original dopant blend layer. Furthermore, the F and CN signals show two tails

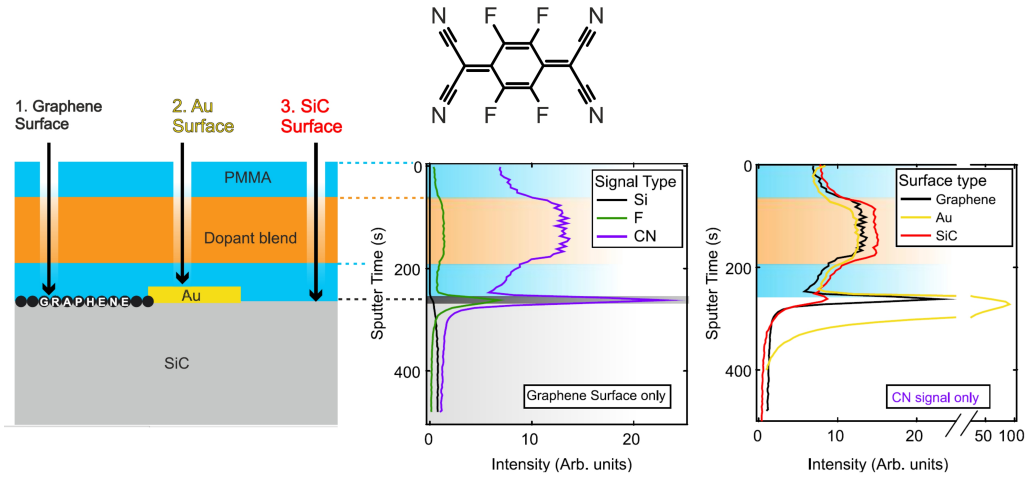


**Figure 4.3:** **Left:** Schematic overview of SiC/G prepared with a PMMA spacer layer, dopant blend and an additional PMMA encapsulation layer. The arrows indicate the three regions which were probed using ToF-SIMS. **Center:** Data measured on the polymer layers above the surface of graphene only. With increasing sputter time the measurement probes deeper into the polymer stack. The plots focus on three signals only: F and CN which indicate the presence of F4TCNQ (top inset), and Si which indicate when SiC has been reached. The F and C signal show that there is a significant amount of F4TCNQ molecules accumulated at the surface of graphene. The diffusion of molecules also occurs towards the upper PMMA surface. **Right:** Focusing only on the CN signal, a comparison between the spatial distribution of F4TCNQ molecules above three regions: Graphene, Au, and SiC is shown. Accumulation of F4TCNQ occurs only on conductive surfaces of graphene and Au, but not on insulating SiC.

originating from the dopant layer, trailing off into the PMMA on both sides, showing that molecules diffuse not only towards graphene but also into the upper PMMA encapsulation layer. It is known that F4TCNQ are mobile in polymers like PMMA, with the diffusion being dependent on polarity and glass transition temperature of the host polymer [47, 48]. Recall that after spin coating of the dopant blend, the samples were baked at 160 °C. This temperature is above the glass transition temperature of PMMA ( $T_G \approx 100^\circ\text{C}$ ), making it easier for molecules to diffuse. The accumulation near graphene is attributed to the formation of a charge-transfer complex between the molecule and graphene. The F4TCNQ remains neutral inside the PMMA [49], but when it encounters a charge donor like graphene the formation of a charge-transfer complex causes F4TCNQ to be bound and stabilized by the Coulomb interaction [50].

Indeed, the same F4TCNQ accumulation can be seen above the surface of Au. The effect here is even stronger than for graphene (3x stronger signal), possibly due to different charge carrier densities and work functions. The area under the accumulation peak is very large compared to the area under the dopant blend, indicating extreme accumulation of F4TCNQ.

A reference measurement was taken above bare SiC, which was exposed through ashing of graphene. Barely any accumulation of F4TCNQ molecules was observed in this region. This behavior is consistent with the notion that the formation of a charge-transfer complex is required in order to capture F4TCNQ molecules.

Because the intensity of the SIMS signal is related to surface density, the data in Figure 4.3 can be used to estimate the surface coverage of F4TCNQ molecules. The time it took to reach the surface (sputter time) can be approximately translated to distance, by matching it to the nominal resist thickness. Then by simply taking the area under the entire SIMS intensity curve, for example for the CN signal, the total amount of F4TCNQ can be calculated (arbitrary intensity units per unit area). The same is done for the area under the accumulation peak near graphene. Experimentally the ratio between the two was found to be around 15 %. This means that 15% of the total amount of F4TCNQ molecules inside the dopant blend layer reached the surface of graphene. With a mixing ratio between F4TCNQ and PMMA of 7 wt.% F4TCNQ in PMMA, density of F4TCNQ  $p = 1.4 \text{ g/cm}^3$ , molar mass  $M = 276 \text{ g/mol}$ , and assuming that the dopant layer is a slab of purely PMMA and F4TCNQ (7 mm x 7 mm x 175 nm), the surface density of F4TCNQ is  $4.6 \times 10^{14} \text{ cm}^{-2}$  or below 5 molecules per  $\text{nm}^2$ . This is comparable to what was estimated from electrical transport measurements.

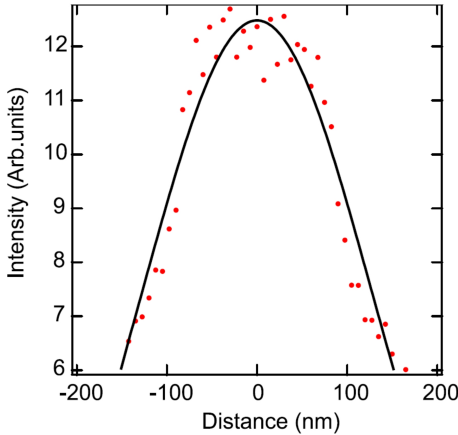


Figure 4.4: The red dots indicate the CN signal extracted from SIMS for chemically doped graphene. The x-axis is the distance, translated from sputtering time. The intensity on the y-axis represents surface concentration at a certain distance. The peak is centered on the 175 nm wide dopant layer, which after 6,000 seconds of annealing at 160 °C, shows diffusion of F4TCNQ going into the PMMA layers to the side. The black solid line is a fit to the surface concentration of an instantaneous extended source, from which the diffusion coefficient was determined to be  $D \approx 10^{-14} \text{ cm}^2/\text{s}$  (in PMMA at 160 °C).

From the CN signal the diffusion coefficient of F4TCNQ through PMMA, at 160 °C can be estimated. Again, assuming that the SIMS is an accurate representation of surface concentration of F4TCNQ, and that sputter seconds corresponds well to distance. Using

Fick's laws for diffusion to model the case of an instantaneous extended limited source diffusion yields the following equation [51]:

$$\frac{c(x,t)}{C_0} = \frac{1}{2} \left\{ \operatorname{erf} \frac{h-x}{2\sqrt{Dt}} + \operatorname{erf} \frac{h-x}{2\sqrt{Dt}} \right\} \quad (4.1)$$

Where  $c(x,t)$  is the surface concentration at position  $x$  (origin in the center of the source) and time  $t$ ,  $C_0$  the initial surface concentration,  $2h$  is the width of the extended source, and  $D$  is the diffusion coefficient. Figure 4.4 shows data of the CN signal measured over the surface of graphene. For simplicity sake the focus has been put on the dopant layer (extended source) and its immediate surroundings (roughly halfway inside the top and bottom PMMA layer). Notably the accumulation layer around graphene has been omitted. By fitting Equation 4.1 using a 175 nm wide source and 6,000 seconds (5 min baking for dopant layer, 5 min for top PMMA layer) the diffusion coefficient was determined to be  $D \approx 10^{-14} \text{ cm}^2/\text{s}$  (in PMMA at 160 °C). Note that the model assumes that the total number of F4TCNQ in the region of interest is constant, which is not true, partly because of accumulation at graphene but also because of the possibility of FTCNQ leaving the polymer entirely. Neat F4TCNQ is known to sublime already at 80 °C, and while more stable in a polymer, extended annealing can still reduce the total amount of F4TCNQ [47].

An estimate for the flux of F4TCNQ molecules to the graphene surface is  $j = D \frac{\Delta c}{\Delta d} = 1.5 \times 10^{-13} \text{ mol/cm}^2\text{s}$ , where  $\Delta c = 2.7 \times 10^{-4} \text{ mol/cm}^3$  is the initial concentration gradient and  $\Delta d = 185 \text{ nm}$  the distance between the center of the source and graphene surface (100 nm is PMMA spacer). This means that  $4.6 \times 10^{14} \text{ cm}^{-2}$  of F4TCNQ reached the graphene within 5,000 seconds, which corresponds well with 6,000 seconds baking time. The time is a rough estimate partly because the accumulation at the graphene surface and the diffusion into the upper PMMA layer have been ignored.

### 4.2.3 Tuning Doping via Thermal Annealing

One experimental observation is that the p-doping effect of F4TCNQ is actually more pronounced for baking times below 5 min. This fact complicates the simple analysis in the previous chapter. Figure 4.5 shows charge carrier density extracted from Hall measurements versus annealing time at 160 °C for a SiC/G covered by a PMMA spacer and dopant blend. At low annealing times the sample is p-doped, and as the time is increased it irreversibly becomes n-doped. From the  $\rho_{XX}$  vs carrier density plot the clear shape of the Dirac peak can be seen, and charge neutrality is reached after 4 min. In a span of 12 minutes the charge carrier density changes almost by  $10^{12} \text{ cm}^{-2}$ , which is 10 % of the total doping strength  $10^{13} \text{ cm}^{-2}$ . This behavior can be speculated to be due to the molecules changing conformation, which affects charge-transfer [52]. They could also be leaving the graphene surface and diffusing away to Au surfaces nearby or even completely leaving the sample [47, 50]. Quantum Hall measurements were performed for each annealing time and the general trend is that quantization is not perfect at the lower annealing times. Samples usually require 4-5 min of annealing before they exhibit well-developed QHE at low doping levels. This is a hint that there is a time scale for F4TCNQ to rearrange near graphene and to provide homogeneous doping.

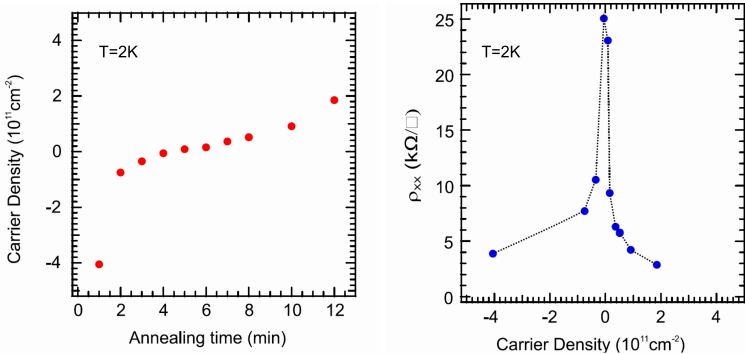


Figure 4.5: Annealing of a SiC/G Hall bar sample prepared with PMMA spacer and dopant blend. The dopant blend has been annealed at 160 °C from 1 min to 12 min. **Left:** Charge carrier density versus annealing time shows that SiC/G becomes more n-doped with annealing time. Charge neutrality is crossed after 4 min of annealing. **Right:**  $\rho_{xx}$  versus charge carrier density has the typical Dirac peak shape. The maximum resistance is reached after 4 min, with a value close to  $h/e^2$ .

As touched upon in Subsection 4.2.1 the diffusion of F4TCNQ molecules was observed to be insensitive to thickness variations of the spacer layer between 100 – 400 nm. After 5 min of annealing all samples showed similarly low doping levels. This hints at that the initial diffusion of F4TCNQ is very fast (high p-doping initially), and is then slightly modulated by subsequent annealing (10 % change in total doping strength).

To test the limit of how thin the resist could be a sample prepared with spacer PMMA layer and dopant blend, annealed for 5 min, was ashed using oxygen plasma. The ashing removed the residual dopant layer and thinned down the PMMA spacer, with the final thickness of only 50 nm. Note that the doping effect of SiC/G was preserved, owing to the accumulation of F4TCNQ near graphene. In fact the samples treated this way become slightly more p-doped. With this extremely thin resist, the increase of n-doping with annealing time is greatly sped up. After just 1 min of baking the carrier density changed on the order of  $4 \times 10^{11} \text{cm}^{-2}$ . This is a sign that the polymer layers are suppressing the diffusion of F4TCNQ away from graphene. This may explain why when only the dopant blend is used the charge carrier density is not as low as with the spacer included, despite both dopant blends being annealed for the same amount of time.

Due to the need for thermal annealing to activate diffusion. the doping effect was found to be significantly stable under ambient conditions. The measurements in Figure 4.5 were all performed on the same sample, showing resilience to thermal cycling. Furthermore, a sample kept in a simple nitrogen closet at room temperature was observed to retain its low doping level for two years (thus far) as shown in Figure 4.6. Different encapsulation schemes were tested, and samples with thicker and/or multiple layers of encapsulation were more stable over time. The most stable samples were covered by five layers of polymers: PMMA-Dopant-PMMA-Dopant-PMMA. Over the course of two year the doping strength degraded by  $\ll 1\%$  (i.e. the change of carrier density  $\ll 10^{11} \text{cm}^{-2}$ ). However, even

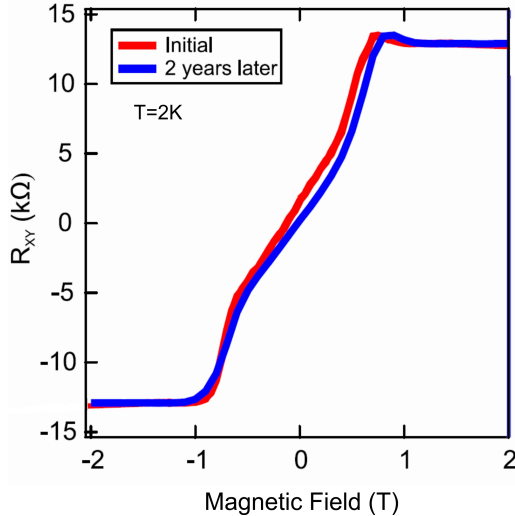


Figure 4.6: A long-term stability comparison measurement taken approximately two years apart for a chemically doped SiC/G Hall bar. For extra protection the sample was covered with two additional PMMA layers and an extra layer of the dopant blend. The total polymer stack looks like PMMA-Dopant-PMMA-Dopant-PMMA. The sample was kept primarily at ambient conditions inside a simple nitrogen box. During this time the carrier density changed only from  $n = 5.3 \times 10^{10} \text{ cm}^{-2}$  to  $n = 6.2 \times 10^{10} \text{ cm}^{-2}$ .

samples with just the standard PMMA spacer and dopant blend were significantly stable, and keep their low doping level  $n \approx 10^{10} \text{ cm}^{-2}$  for at least six months, with little sign of degradation. Note that the full polymer stack is used for samples with an electrostatic top gate.

#### 4.2.4 Macroscopic Homogeneity

The measurements presented in Subsection 4.2.1 were performed on microscopic Hall bar devices with  $W=2\text{-}100 \mu\text{m} \times L=10\text{-}300 \mu\text{m}$ . Chemical doping of macroscopic hall bars  $W=5 \text{ mm} \times L=5 \text{ mm}$  was also investigated. Figure 4.7 shows quantum Hall measurements on a macroscopic SiC/G Hall bar device prepared with PMMA spacer and dopant blend, according to the standard recipe. The linear low-field  $R_{XY}$  [22, 53–55] and the well developed QHE below 2 T with  $\rho_{XX} = 0$  indicate that the device acts like a system with a single band, with spatially homogeneous charge carrier density [21, 56]. The charge carrier density is  $p = 9 \times 10^9 \text{ cm}^{-2}$ , hole doped, and mobility is  $\mu = 39,000 \text{ cm}^2/\text{Vs}$ . The low macroscopic charge disorder and high mobility shows that the doping technique is promising for wafer-scale applications. The slight difference in final charge carrier density compared to devices in Subsection 4.2.1 could be due to natural sample variations, and because a different spacer layer was used (PMMA vs copolymer PMMA). Note that the slight asymmetries in the data, especially around zero field  $\rho_{XX}$ , are attributed to presence of steps in SiC substrate, bilayer inclusions, and other defects. These effect can

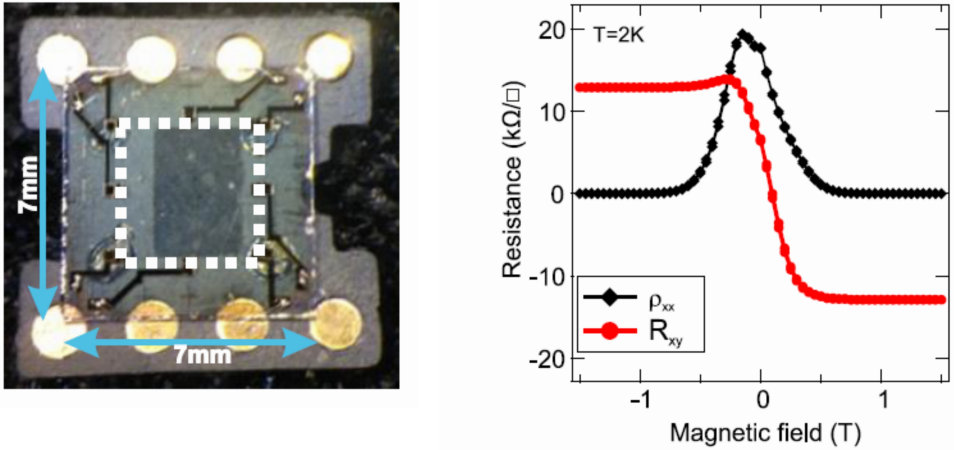


Figure 4.7: **Left:** Optical image of a macroscopic SiC/G Hall bar device with  $W=5$  mm  $\times$   $L=5$  mm. The white dotted line indicates extent of the square graphene Hall bar. Eight circular contact pads are connected to graphene through thin leads. **Left:** Magnetotransport measurement of the QHE performed at 2 K. The linear low-field  $R_{XY}$  and the well developed QHE below 2 T with  $\rho_{XX} = 0$  indicate that the device is homogeneously doped. The charge carrier density is  $p = 9 \times 10^9 \text{ cm}^{-2}$ , hole doped, and mobility is  $\mu = 39,000 \text{ cm}^2/\text{Vs}$ .

be mitigated for microscopic hall bars by careful placement, but impossible to avoid for a device which spans the entire chip.

#### 4.2.5 Microscopic Homogeneity

An electrostatic gate was deposited on top of the polymer stack in order to further study the electron transport properties of doped SiC/G close to the charge neutrality point. While the charge carrier density can be tuned using annealing, it is much more convenient to use an electrostatic gate. Due to the reduced gate efficiency and thick dielectric, the total change of charge carrier density induced by the gate is only on the order of  $\Delta n = 10^{11} \text{ cm}^2$ , within the tested range of gate voltages  $V_G = -50 \text{ V}$  to  $+200 \text{ V}$ . However, it is still sufficient to be able to tune the charge carrier density of SiC/G across the Dirac point since SiC/G has already been brought close to charge neutrality by F4TCNQ. Figure 4.8 shows  $\rho_{XX}$  as a function of applied gate voltage  $V_G$ . The Dirac point is reached at around  $V_G = -40 \text{ V}$  and  $\rho_{XX}$  has a value close to  $h/2e^2$ . The allowed gate voltages before breakdown of the dielectric occurs is asymmetric around the Dirac point. This is likely due to the already induced electric field from F4TCNQ dopant near graphene. For each gate voltage a full quantum Hall measurement was performed. Two examples close to the Dirac point are given in Figure 4.8. At  $V_G = -53 \text{ V}$  the sample shows p-type behavior with  $p = 5.6 \times 10^9 \text{ cm}^{-2}$  and mobility  $\mu = 52,000 \text{ cm}^2/\text{Vs}$ . At  $V_G = -23 \text{ V}$  the sample shows n-type behavior with  $n = 6.4 \times 10^9 \text{ cm}^{-2}$  and mobility  $\mu = 61,000 \text{ cm}^2/\text{Vs}$ .

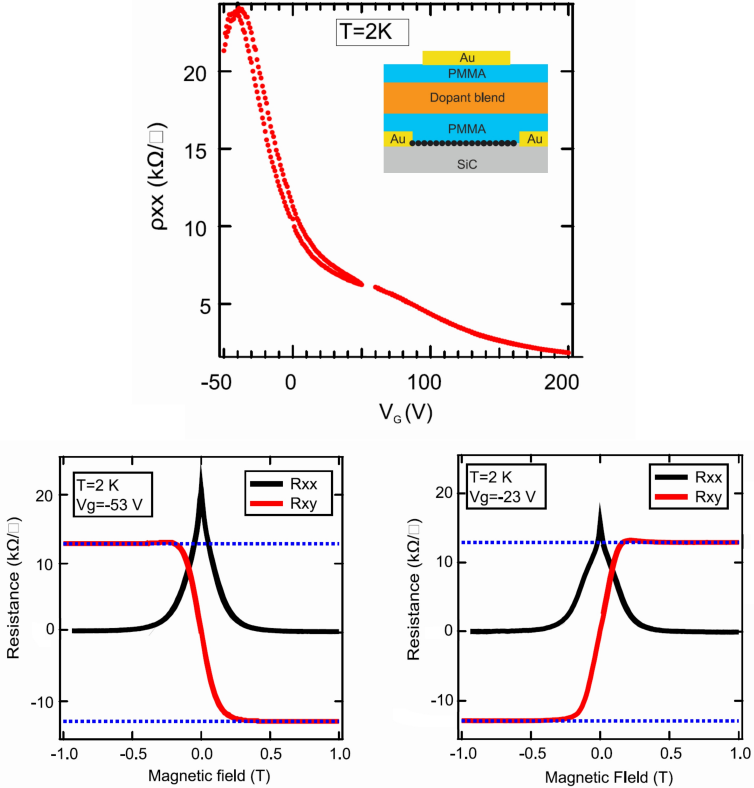


Figure 4.8: **Top:**  $\rho_{XX}$  measured as a function of applied gate voltage. The Dirac peak is reached at  $V_G = -40$  V. The inset shows a schematic representation of the top gated, chemically doped, SiC/G. For each gate voltage point a full quantum Hall measurement was performed.  $\rho_{XX}$  is the zero-field resistance, measured at 2 K. **Bottom:** Fully developed QHE for charge carrier densities close to the Dirac point. The blue dotted lines mark the position of  $\pm h/2e^2$ . At  $V_G = -53$  V the sample shows p-type behavior with  $p = 5.6 \times 10^9 \text{ cm}^{-2}$  and mobility  $\mu = 52,000 \text{ cm}^2/\text{Vs}$ . At  $V_G = -23$  V the sample shows n-type behavior with  $n = 6.4 \times 10^9 \text{ cm}^{-2}$  and mobility  $\mu = 61,000 \text{ cm}^2/\text{Vs}$ . The charge puddle regime lies in between these points, and for those gate voltages the charge carrier density and mobility cannot be determined from Hall measurements due to non-linear low-field  $R_{XY}$ .

In both of these cases the QHE is well-developed, like is the case for a macroscopic Hall bar, which means that even at these low carrier densities the sample has yet to enter into the charge puddle regime. For charge densities even closer to the Dirac point the QHE starts to be affected by the charge inhomogeneity, and  $R_{XY}$  is no longer linear at low-field and  $\rho_{XX}$  is no longer zero at high fields. The charge carrier density and mobility for these gate voltage is therefore undefined, and omitted from future plots.

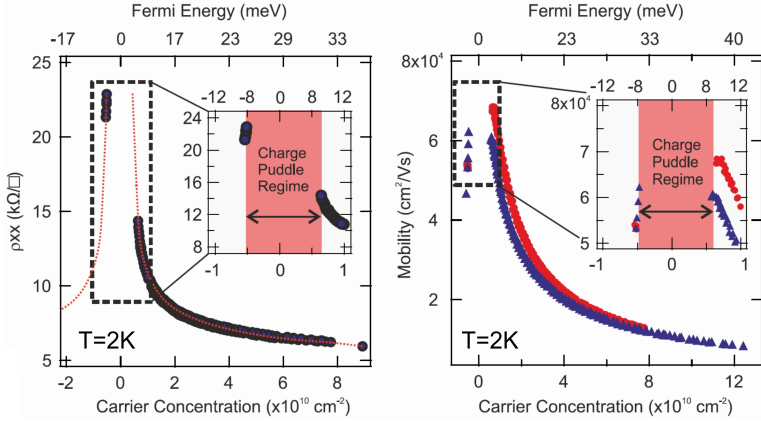


Figure 4.9: **Left:**  $\rho_{XX}$  versus charge carrier density, extracted from QHE measured at different gate voltages. There is a clear Dirac cone shape (red line is a guide to the eye). The omitted data indicate the charge puddle region where Hall measurements become unreliable due to charge disorder. The extent of this region is  $\approx \pm 9$  meV around charge neutrality. **Right:** Carrier mobility versus carrier density, measured at two places on the same chip (red and blue). The mobility reaches  $70,000 \text{ cm}^2/\text{Vs}$  close to the Dirac point.

Figure 4.9 shows the extracted charge carrier density and mobility for the gate sweep. The missing data near neutrality marks the charge puddle region.  $\rho_{XX}$  versus charge carrier density  $n$  reproduces the shape of the Dirac cone. The peak is very sharp, i.e. the charge puddle regime is narrow in terms of energy. Assuming that the minimum SiC/G charge carrier density for well-developed QHE marks the boundary of the charge puddle regime, the strength of charge puddle fluctuations is then  $\approx \pm 9$  meV. Mobility versus carrier density shows that at the lowest doping level the maximum mobility reaches  $70,000 \text{ cm}^2/\text{Vs}$ . The blue and red curves denote measurements performed at two different places on the same chip.

To confirm the measured charge disorder strength of  $\approx \pm 9$  meV the two-band model of disorder-induced temperature dependent transport is used [32, 34]. By performing Hall measurements at various temperatures, and fitting the temperature dependence of (effective) charge carrier density to Equation 2.33, the disorder strength  $s$  can be determined. The parameter  $s$  corresponds to the average strength of spatially distributed charge disorder, i.e. charge puddles. Figure 4.10 shows an example of a measurement fitted to the model, and they agree well with each other. Four different samples were investigated this way and the average disorder strength is  $s = 7.7 \pm 1.2 \text{ meV}$ , where the error bar denotes two standard deviations. This is in good agreement from the gating experiment above, in which the charge puddle strength was found to be  $\approx \pm 9$  meV. The mobility ratio between electron and holes show that electrons have  $\approx 50\%$  higher mobility. This explains the higher mobility for electrons compared to holes, despite a higher electron carrier density, seen in Figure 4.9.

As an aside, the gate allowed for the investigation of temperature dependence of resistance close to charge neutrality. Figure 4.11 shows a comparison between non-gated

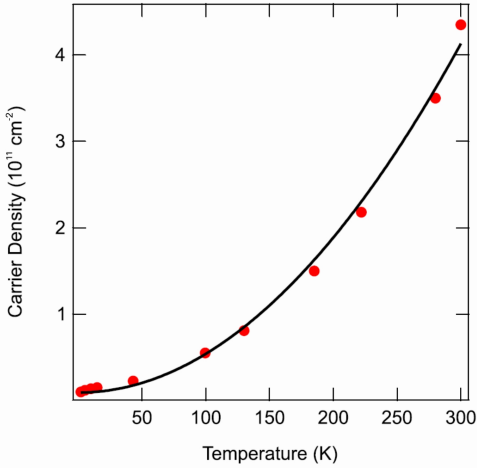


Figure 4.10: Temperature dependence of effective carrier density (red dots) fitted to two-band model of disorder-induced temperature dependent transport in order to extract the disorder strength  $s$ . The average result of fits to four different samples is  $s = 7.7 \pm 1.2$  meV, where the error bar denotes two standard deviations. The mobility ratio is  $u_e/u_h = 1.5$ , with electrons having 50% higher mobility compared to holes.

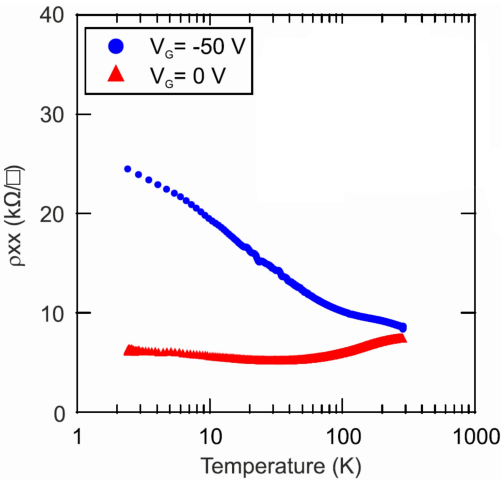


Figure 4.11: Temperature dependence of  $\rho_{XX}$  for two different samples, one with and one without applied gate. The gate voltage is applied starting from 300 K and kept constant throughout the cool down process. With the high applied gate voltages the sample is charge neutral (in charge puddle regime) and the resistance increases monotonously with temperature.

device versus the gated one. The non-gated device shows a slight hump in resistance close to 300 K, similar to Figure 4.2, but with the difference that this particular sample has higher n-doping. For the gated sample the resistance simply increases monotonously with temperature. This is a sign of very low doping, and Hall measurements showed that the sample was indeed in the charge puddle regime.

#### 4.2.6 Grazing-incidence Wide-angle X-ray Scattering

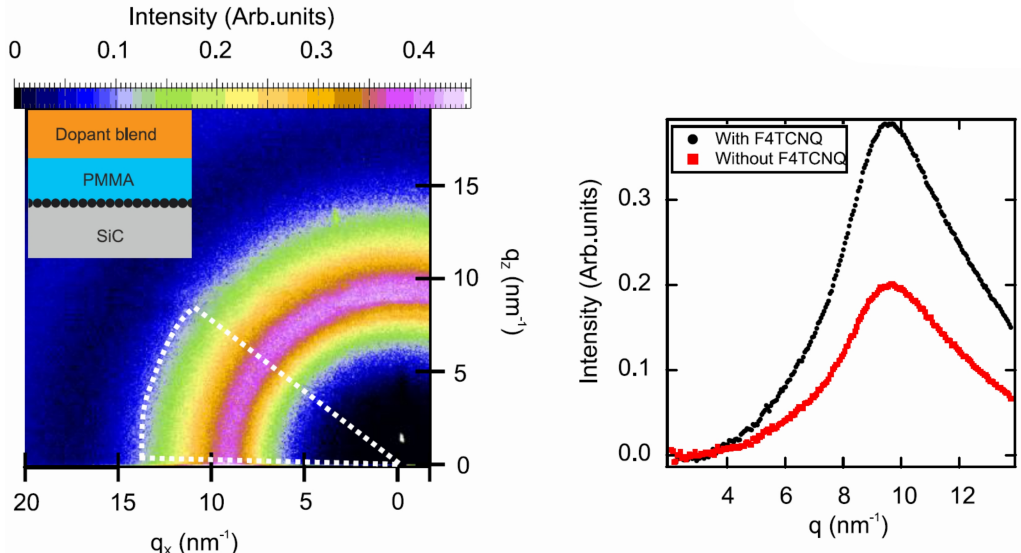


Figure 4.12: **Left:** 2D plot of room temperature GIWAXs intensity. The inset shows the measured sample, with PMMA spacer and dopant blend. The incident angle was 0.15 degrees. A diffuse background has been subtracted. There is a clear halo with radius  $q = 9.6 \text{ nm}^{-1}$ . The white dotted line indicate the region where the data was integrated over azimuthal angles to produce an intensity profile. **Right:** Intensity profile shows a broad diffraction peak at  $q = 9.6 \text{ nm}^{-1}$ . The red curve shows a reference measurement taken on a sample prepared using a dopant blend without F4TCNQ (neat PMMA). The peak remains which means that it belongs to PMMA itself. The addition of F4TCNQ enhances the signal twofold.

Grazing-incidence Wide-angle X-ray Scattering (GIWAXs) was performed to shed more light on the dispersion of F4TCNQ dopants in the PMMA matrix. The measurements were performed at room temperature under ambient conditions. Figure 4.12 shows the 2D spectra collected at 0.15 degrees incident angle for chemically doped SiC/G using the standard recipe with PMMA spacer and dopant blend. Incident angles between 0.1-0.25 degrees were tested but no significant change in features were observed. Starting from 0.125 degrees angle the attenuation length of the x-ray (0.1162 nm wavelength) in PMMA is already 500 nm, enough to penetrate the entire polymer stack. A background from

diffuse scattering has been subtracted and the only visible feature is a broad amorphous halo, with a diffraction peak at  $q = 9.6 \text{ nm}^{-1}$ . The origin of this peak comes from PMMA itself, as verified by a reference measurement using PMMA spacer with neat PMMA on top. Interestingly, the addition of F4TCNQ enhances the signal by a factor of two, but creates no additional diffraction spots.

The enhancement of the original PMMA peak due to F4TCNQ implies that the molecules either stabilize the polymer backbone or follow the packing of PMMA itself (possibly both). The characteristic length-scale of the PMMA-F4TCNQ system is 6.6 nm. Assuming that F4TCNQ obeys this packing even at the accumulation layer, then the surface coverage is 2-3 F4TCNQ molecules per  $\text{nm}^2$ , which corresponds well to estimates from SIMS and electrical transport. At these high packing densities the conformation of molecules is likely non-planar, i.e. they stand up on the surface of graphene [23].

The lack of distinct diffraction spots suggests that F4TCNQ is well-dispersed in the PMMA matrix, and do not aggregate significantly. Using Scherrer analysis the size of crystallites can be calculated. The Scherrer equation reads  $\tau_c = \frac{\kappa\lambda}{\beta\cos\theta}$ , where  $\tau_c$  is the mean size of crystal domains,  $\kappa$  a dimensionless shape factor (for spherical particle = 0.9),  $\lambda$  x-ray wavelength,  $\theta$  Bragg angle and  $\beta$  the FWHM of the diffraction peak. The average for the coherence length of F4TCNQ crystallites is then  $\tau_c \approx 2 - 3 \text{ nm}$ .

From magnetotransport data the charge homogeneity of F4TCNQ doped SiC/G is clear. One might expect that this order would translate to crystalline F4TCNQ. However, no long range crystalline order was observed at room temperature. It is likely that any signal of the buried accumulation layer, even if it has a different GIWAXs spectra, is drowned out by the signal from the bulk dopant blend layer. The signal could also be smeared by thermal fluctuations. GIWAXs measurements would need to be performed at cryogenic temperatures to mimic the conditions of QHE measurements. However, there are other mechanisms whereby charge homogeneity could be achieved, without crystalline order of F4TCNQ itself. For instance, the combination of low charge carrier density of SiC/G, with increasing impurity density (i.e. addition of densely packed F4TCNQ molecules) can suppress charge scattering in SiC/G if the spatial correlation between impurities is strong enough [57, 58]. GIWAXs reveals the possibility of PMMA playing the role of a template for the packing of F4TCNQ, with a characteristic length scale of 6.6 nm. In fact, the packing density of F4TCNQ, assuming a characteristic length scale of 6.6 nm, translates to 2-3 molecules per  $\text{nm}^2$  which is consistent with both SIMS and magnetotransport estimates. Another mechanism which could explain the low charge disorder is thermally induced redistribution of charges in the dopant layer under the effect of electric fields, which can screen charge inhomogeneity in graphene [59]. Indeed, the next section will reveal that F4TCNQ remains mobile in PMMA even at low temperatures.

#### 4.2.7 Redistribution of Dopants

To investigate the movement and redistribution of F4TCNQ dopants a positive gate voltage was applied to a chemically doped sample at room temperature, and kept while the sample was cooled down to 2 K, similar to the measurement presented in Figure 4.11. A positive gate voltage increases the n-doping, and thus decreases the measured resistance. Once the sample reached 2 K the gate was turned off. The resistance is immediately

increased due to the removal of the external gate. However, the frozen F4TCNQ molecules effectively retained some of the initial field. Figure 4.13 starts immediately after the gate has been turned off. The resistance is at point A. The sample is heated up to point B and then cooled down back to point A. During this time any hysteresis in resistance was monitored, which is a sign that F4TCNQ molecules are mobile. The process is repeated with progressively higher temperatures, always returning to 2 K. Once the sample reached 250 K a clear hysteresis was seen, with the new resistance at 2 K being point F. The higher resistance value signals the release of some of the trapped field due to charge redistribution. The sample was completely recovered to its initial, non-gated state, after being kept at 300 K for an extended period of time. A closer look reveals that there are signs of hysteresis at much lower temperatures, already from around 100 K.

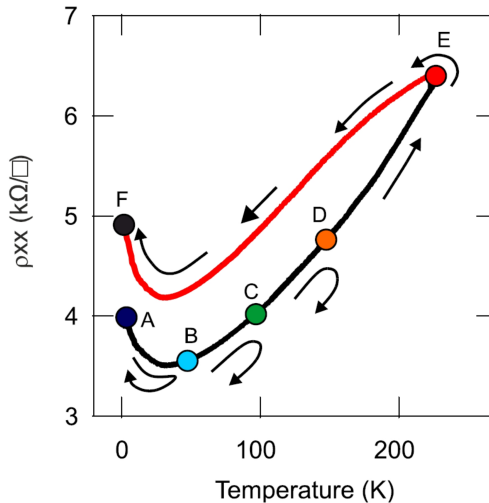


Figure 4.13: The electric field from an electrostatic top gate was frozen into F4TCNQ dopants. The initial field, +50 V, was applied at 300 K and kept during cool down. Once at 2 K the gate was turned off. The resistance changed to the value at point A. Starting from point A at 2 K temperature sweeps, trace and retrace, were performed to successively higher temperatures. After temperature sweeps to point B 50 K, point C 100 K, point D 150 K the resistance returned to its value at point A. Clear hysteresis in resistance, i.e. charge redistribution, was clearly observed only from 250 K. The behavior in temperature irreversibly switched from the back curve to the red one, with the resistance at 2 K change to a higher value.

A more careful measurement of the redistribution of F4TCNQ was performed by switching the gate voltage abruptly at different temperatures and monitoring the transients in resistance as F4TCNQ responded to the applied field. Figure 4.14 shows the experiment where the gate was switched abruptly to  $V_G = -5$  V (the response is symmetric for positive gates). The time evolution of resistance  $\rho_{XX}$  was monitored as a function of time. The negative voltage induces less n-doping, thus increasing resistance for the initially

slowly n-doped sample. The initial response to the gate is fast ( $< 2$  s), which includes the response of graphene itself, RC-constants etc. There is a much slower transient which was monitored for 200 s after the fast transients have died out. This slower transient is attributed to the slower movement of F4TCNQ molecules. The measurement was repeated for several temperatures, from 200 K down to 100 K. As the temperature decreases the time constant for the transient increases, indicating the freezing of F4TCNQ motion. At 113 K the molecules appear to be almost completely frozen, at least on the time scale of 200 s. The time dependence is logarithmic for all tested temperatures. Logarithmic time dependence of charge redistribution is typical for glass type of disorder [60], which is the type of disorder expected for polymer based dopant blends. Note that the measurement setup is sensitive to time drift due to the small change in resistance ( $< 5\%$  relative to the initial change immediately after the gate was turned on. All curves have a slight slope of decreasing resistance due to temperature drift. This is most visible for the x10 zoomed in curve at 113 K.

The thermal energy scale for F4TCNQ movement  $\approx 10$  meV is in notable coincidence with the measured charge disorder  $\pm 9$  meV. This could indicate that F4TCNQ indeed screens charge disorder, but only up to the temperatures were they are still mobile.

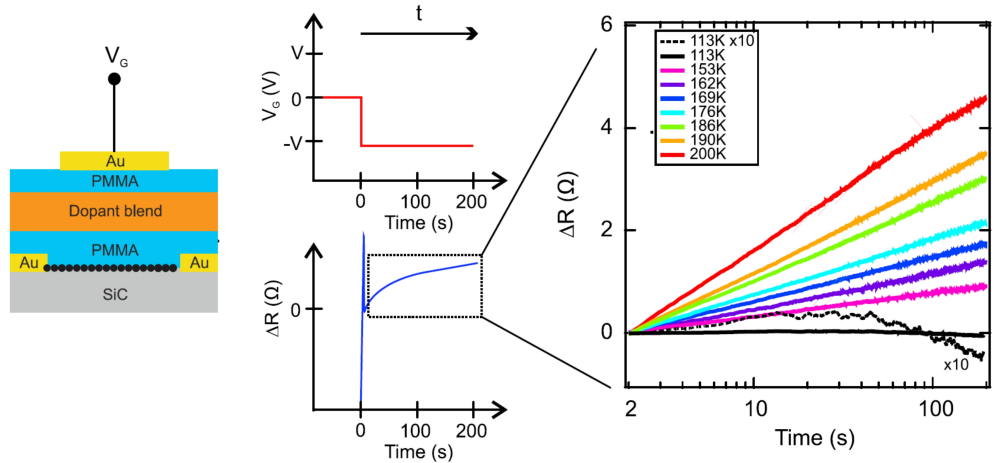


Figure 4.14: **Left:** Schematic representation of chemically doped SiC/G with an electrostatic top gate. **Center:** Schematic representation of the measurement procedure. When gate voltage is switched to a negative voltage the doped sample responds, leading to an increase in resistance. After fast transients such as graphene response, and RC-constant, have settled down ( $< 2$  s) a slower transient appears. This transient is attributed to charge redistribution due to F4TCNQ. **Right:** The slower transient is monitored for 200 s. Note that the relative change in resistance during this time is  $< 5\%$  of the total change immediately after the gate was switched on. The transient shows logarithmic time dependence, and appears to freeze out at 113 K.

## 4.3 Initial Metrological Tests

The previous section was primarily focused on chemically doped samples close to the charge neutrality point. For real-world applications as QHR standards the desired charge carrier density is on the order of  $2 \times 10^{11} \text{ cm}^{-2}$ . This carrier density will ensure that the critical current is maximized for operation at 4 K and 5 T [17]. The samples in this section were prepared using PMMA spacer, dopant blend and an additional encapsulation layer for added stability. The added encapsulation layer adds 5 min extra to the annealing time, conveniently bringing the final charge carrier density close to the desired value (see Figure 4.5). If needed fine-tuning can be made by annealing in smaller increments until the desired carrier density has been reached. To test the metrological viability of the F4TCNQ doping method the value of the  $R_{XY} = h/2e^2$  plateau of chemically doped SiC/G has to be compared to a conventional GaAs based QHR standard. An indirect comparison is achieved by first comparing GaAs to a standard  $100 \Omega$  resistance, and then SiC/G to the same resistor. These measurements requires a CCC in order to achieve precision measurements with uncertainty on the order of n $\Omega/\Omega$  (part-per-billion).

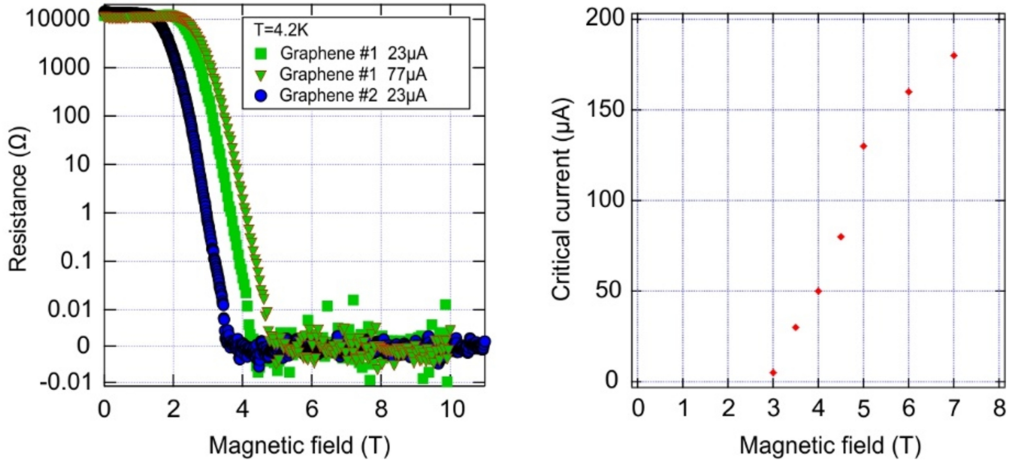


Figure 4.15: **Left:** Quantum hall measurements at 4.2 K, showing only  $\rho_{XX}$ , for chemically doped samples. Their charge carrier densities have been tuned to be  $2 \times 10^{11} \text{ cm}^{-2}$ . **Right:** Critical current as a function of magnetic field for Graphene #2. The width of the Hall bar is 30  $\mu\text{m}$ .

The first step is to verify that the sample is in operating condition. Figure 4.15 shows quantum Hall measurements for two samples. This test assesses whether the samples show QHE by looking at if  $\rho_{XX} = 0$ , at 4.2 K. For practical purposes the minimum magnetic field should also be low, but for an initial test run the full range of field, up to 11 T, is used. The critical current, i.e. the maximum current before QHE is destroyed due to overheating of the electron system, and its dependence on magnetic field was also determined (shown only for Graphene #2). The maximum current is determined by at

what current  $\rho_{XX}$  increases above the noise level of the measurement ( $0.01 \Omega$  in this case). A higher current is always more desirable in order to reduce noise, but  $23 \mu\text{A}$  was more than sufficient for these measurements.

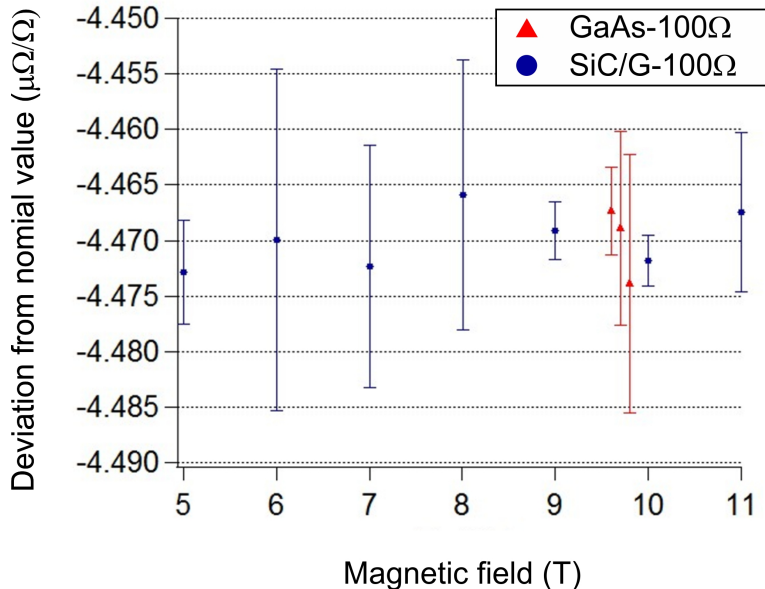


Figure 4.16: Comparison measurements between GaAs-100  $\Omega$  and SiC-100  $\Omega$ . The y-axis plots the measured relative deviation of the 100  $\Omega$  standard from its nominal value of 100  $\Omega$ , as compared to the QHR standard. GaAs was measured at 1.7-1.9 K, with a magnetic field slightly below of 10 T. SiC/G was measured at 4.2 K and in a wide range of magnetic fields from 5 to 11 T. The bias was  $23 \mu\text{A}$  for both samples.

First the GaAs QHR standard was brought into quantizing conditions ( $\nu = 2 R_{XY} = h/2e^2$ ) and compared to the 100  $\Omega$  resistor using the CCC. Due to the comparatively low LL energy spacing GaAs needs to operate at a temperature of 1.7-1.9 K, with a magnetic field slightly below of 10 T. The bias current was  $23 \mu\text{A}$ . A common procedure is to repeat the comparison measurement at several different magnetic fields along the plateau. This functions both as an additional test of the QHE (plateau should be flat) and as a way to collect more data for averaging. Since the GaAs plateau is relatively narrow, only three different magnetic fields were tested. The same procedure was then repeated for the F4TCNQ doped SiC/G QHR standard. Due to the advantages of SiC/G the sample was measured at 4.2 K and in a wide range of magnetic fields from 5 to 11 T. The bias current was still  $23 \mu\text{A}$ .

Figure 4.16 shows the results of the comparison measurements between GaAs-100  $\Omega$  and SiC-100  $\Omega$ . The y-axis plots the measured relative deviation of the 100  $\Omega$  standard from its nominal value of 100  $\Omega$ , as compared to the QHR standard, which is assumed to have a resistance of exactly  $h/2e^2$ . It can be seen that SiC/G is truly quantized in the full range of magnetic field. It is also clear that, within the measurement error,

that the value of the  $R_{XY}$  plateau for GaAs and SiC/G agree well with each other. By taking the mean relative deviation as measured for SiC/G, across all magnetic fields, and comparing it to the corresponding value for GaAs, the discrepancy between the two is  $\Delta_{SiC/G-GaAs} = 0.0 \pm 4.5 \text{ n}\Omega/\Omega$ . The error bar signifies two standard errors of the mean. This is promising for the viability of F4TCNQ doped SiC/G in quantum resistance metrology.

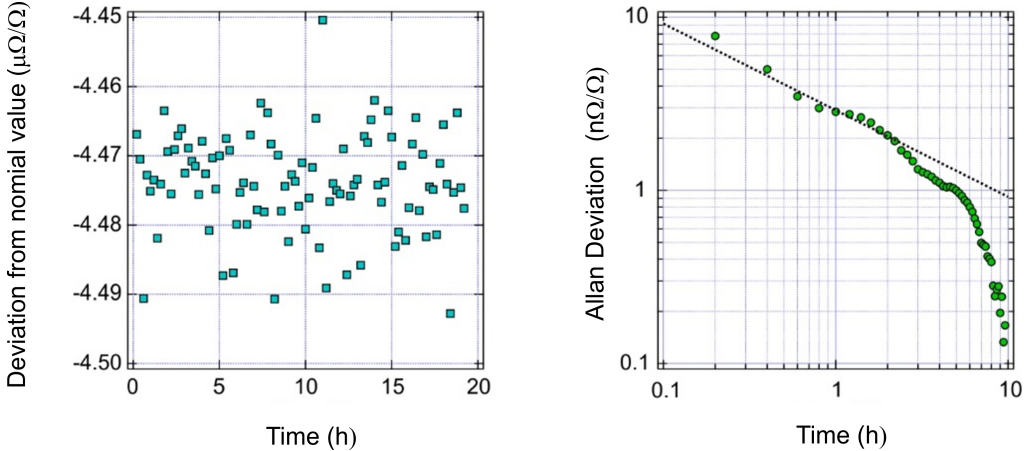


Figure 4.17: **Left:** Prolonged, continuous, CCC measurement between F4TCNQ doped SiC/G and  $100 \Omega$  standard performed at 4.2 K, 8 T and  $23 \mu\text{A}$  bias. Each point corresponds to 12 min of measurement. **Right:** Allan deviation extracted from the time series. The black dotted line is a fit to  $\approx t^{-0.5}$ , which indicates uncorrelated white noise.

The aforementioned data were collected with relatively low number of averages, due to it being a trial run. The measurement uncertainty can be reduced through additional averages. Figure 4.17 shows a prolonged CCC measurement, comparing F4TCNQ doped SiC/G to  $100 \Omega$  standard, at 4.2 K, 8 T and  $23 \mu\text{A}$  bias. The measurement was performed continuously for up to 20 hours. From this data the Allan deviation can be calculated [61]. The Allan deviation is seen to be decreasing with time as  $\approx t^{-0.5}$  which is an indication of uncorrelated white noise being the dominating source of measured uncertainty. This means that the uncertainty can be decreased through additional measurements. The noise level could realistically be decreased to  $0.5 \text{ n}\Omega/\Omega$ .



## 5 Conclusions and Outlook

In summary, the work presented in this thesis concerns itself with SiC/G based QHR standards. In the pursuit of a more practical realization of a QHR standard, which utilizes the special properties of SiC/G, the need for a stable, potent, reliable and tuneable doping method to control the charge carrier density was made apparent. To that end, a new chemical doping method using F4TCNQ was investigated. The effects of F4TCNQ on SiC/G were known previously, but the ambient instability of doping obscured investigations into macroscopic electron transport phenomena. By introducing PMMA as a host matrix, forming a dopant blend consisting of F4TCNQ and PMMA, air-stable doping of SiC/G was achieved, with long-term stability of over two years when kept in a simple nitrogen enclosure. It was found that this dopant blend could bring SiC/G close to charge neutrality, due to the fact that F4TCNQ molecules diffuse through PMMA and preferentially accumulate near the surface of graphene, forming a charge-transfer complex. The doping, both on the microscopic and macroscopic scale, was found to be significantly homogeneous, with the strength of charge disorder being  $\approx \pm 9$  meV and carrier mobilities up to  $70,000$  cm $^2$ /Vs. This low disorder is comparable to state-of-the-art graphene devices based on hBN encapsulated flakes or suspended graphene. However, in contrast to those methods the chemical doping technique was shown to be scalable, with tested devices being up to millimeter scale. The method is easy to use, requiring only spin coating of a PMMA spacer layer and subsequently the dopant blend on SiC/G. The final charge carrier density of doped samples can be tuned using thermal annealing at 160 °C to suit the desired application and operating regime for QHE measurements. Initial test of the metrological viability of doped SiC/G QHR standards are promising. The value of quantized resistance  $h/2e^2$  between chemically doped SiC/G and a GaAs-based QHR standard was measured differ by  $\Delta_{SiC/G-GaAs} = 0.0 \pm 4.5$  nΩ/Ω, indicating excellent agreement. Further metrological trials are required to collect more statistics over device performance and reproducibility, study long-term stability (which is decades for GaAs), and the limits of the parameter space for operation. The aforementioned tasks are more related to engineering, but from a theoretical standpoint there are still many unanswered questions regarding the exact mechanism behind the diffusing and accumulation of F4TCNQ, and how they lead to the extraordinarily homogeneous doping of SiC/G.

While electrical transport measurements at cryogenic temperatures unequivocally demonstrated the homogeneous doping of SiC/G, the underlying reason could not be fully determined. One missing piece of this puzzle is the exact packing and conformation of F4TCNQ molecules on SiC/G. SIMS revealed that F4TCNQ molecules accumulate near the surface of graphene, but the conformation of molecules is not known. The estimated surface coverage from electrical transport and SIMS (and even GIWAXs) suggests a high packing density of up to 2-5 molecules per nm $^2$ , which from the size of the F4TCNQ molecules implies non-planar adsorption. GIWAXs was used in an attempt to find long-range order of F4TCNQ in the thin accumulation layer, and their packing density and direction, in order to try and provide answers to these questions. Unfortunately, due to the thin accumulation layer of F4TCNQ being buried underneath thick polymer, the

measurement was obscured by the bulk dopant blend and PMMA layers. Furthermore, only room temperature measurement at ambient conditions were available, thus further smearing any potential sharp diffraction spots due to crystalline F4TCNQ (if it is there). As discussed, charge homogeneity can arise from spatially correlated disorder of randomly oriented F4TCNQ, and GIWAXs measurement indicated the possibility of F4TCNQ being packed inside PMMA with a characteristic length scale of 6.6 nm, and size of crystallites being 2-3 nm. However the alternate explanation of long-range ordering of F4TCNQ molecules, i.e. crystal F4TCNQ over large areas, can not be ruled out yet. Future experiments could include cryogenic GIWAXs, scanning probe microscopy with atomic lateral resolution such as scanning tip microscopy, or even transmission electron microscopy. A major hurdle, no matter which technique, is the isolation of the buried accumulation layer from the bulk dopants. Additionally, the dynamics of F4TCNQ diffusion and movement through PMMA, especially close to the accumulation layer, can also be explored further. It was observed that the effect of F4TCNQ doping on SiC/G could be tuned via thermal annealing. The reason is not entirely clear, with the possibilities being a conformal change and/or diffusion away from SiC/G, and possibly leaving the sample entirely due to sublimation. Ideally, the sample would be annealed in-situ and studied in real-time to catch the diffusion dynamics.

Setting aside further experiments to complement the current work, the most exiting future prospect is the exploration of the vast catalog of polymers and organic/organometallic molecules. This novel method is in principle applicable to any combination of a suitable host polymer(s) with a suitable molecule(s), as long as diffusion is allowed. This potentially opens up a scalable route towards expanding the properties of graphene and other 2D materials in general, through molecular functionalization guided by a polymer. One intriguing possibility is the creation and investigation of electron transport in new two-dimensional systems of ordered molecular arrays templated by 2D crystals [62, 63].



# A Recipes

All microfabrication recipes are listed in the sections below.

## A.1 RCA cleaning

Required cleaning step of SiC chips before growth of SiC/G:

- Mix 200 mL deionized water, 40 mL ammonia water ( $\text{NH}_3$  30 wt. %) and 40 mL aqueous hydrogen peroxide ( $\text{H}_2\text{O}_2$  30 wt. %). This mixture is referred to as SC1.
  - Heat to 80 °C on a hotplate.
  - Submerge SiC chips in the heated solution for 10 min.
  - Rinse in deionized water bath.
  - Submerge chip for 30 s in 1:50 aqueous solution of hydrofluoric acid (HF) kept at 25 °C.
- Mix 200 mL deionized water, 40 mL hydrochloric acid ( $\text{HCl}$  37 wt. %) and 40 mL aqueous hydrogen peroxide ( $\text{H}_2\text{O}_2$  30 wt. %). This mixture is referred to as SC2.
  - Heat to 80 °C on a hotplate.
  - Submerge SiC chips in the heated solution for 10 min.
  - Rinse in deionized water bath.
  - Dry using nitrogen gas.

## A.2 Electron Beam Lithography

Three-step process of fabrication of graphene Hall bar devices:

### A.2.1 Anchors

- Spin coat P(MMA-MAA 8.5 %), 6 wt. % in ethyl lactate solvent (COPEL6). At 6,000 rpm for 1 min, the resulting thickness is  $\approx 100$  nm.
  - Bake for 5 min at 170 °C
- Spin coat A-RP 6200.13 dissolved 2:1 in anisole. At 6,000 rpm for 1 min, the resulting thickness is  $\approx 175$  nm.
  - Bake for 5 min at 170 °C

- Expose to e-beam. For large features ( $> 1 \mu\text{m}$ ) use 35 nA beam current and dose of  $600 \mu\text{C}/\text{cm}^2$ . For small features ( $< 1 \mu\text{m}$ ) use 2 nA beam current and dose of  $700 \mu\text{C}/\text{cm}^2$ .
- Develop the top resist layer A-RP using o-xylene developer for 30 s.
- Develop the bottom resist layer COPEL6 using o-xylene developer for 40 s.
- Remove exposed graphene using 1 min of oxygen plasma ashing. 50 W, 250 mT chamber pressure and 10 sccm flow of oxygen.
- Deposit metal using PVD by e-beam evaporation of Ti (5 nm) followed by Au (80 nm).
- Lift-off using acetone.
- Rinse with isopropanol.
- Dry using nitrogen gas

### A.2.2 Contacts

- Spin coat P(MMA-MAA 8.5 %), 6 wt. % in ethyl lactate solvent (COPEL6). At 6,000 rpm for 1 min, the resulting thickness is  $\approx 100 \text{ nm}$ .
- Bake for 5 min at  $160^\circ\text{C}$  (lower temperature because of no ashing step)
- Spin coat A-RP 6200.13 dissolved 2:1 in anisole. At 6,000 rpm for 1 min, the resulting thickness is  $\approx 175 \text{ nm}$ .
- Bake for 5 min at  $160^\circ\text{C}$
- Expose to e-beam. For large features ( $> 1 \mu\text{m}$ ) use 35 nA beam current and dose of  $600 \mu\text{C}/\text{cm}^2$ . For small features ( $< 1 \mu\text{m}$ ) use 2 nA beam current and dose of  $700 \mu\text{C}/\text{cm}^2$ .
- Develop the top resist layer A-RP using o-xylene developer for 30 s.
- Develop the bottom resist layer COPEL6 using o-xylene developer for 40 s.
- Deposit metal using PVD by e-beam evaporation of Ti (5 nm) followed by Au (80 nm).
- Lift-off using acetone.
- Rinse with isopropanol.
- Dry using nitrogen gas.

### A.2.3 Ashing

- Spin coat PMMA, 6 wt. % in anisole (PMMA A6). At 6,000 rpm for 1 min, the resulting thickness is  $\approx$  375 nm.
- Bake for 5 min at 170 °C
- Expose to e-beam. For large features ( $> 1 \mu\text{m}$ ) use 35 nA beam current and dose of 600  $\mu\text{C}/\text{cm}^2$ . For small features ( $< 1 \mu\text{m}$ ) use 2 nA beam current and dose of 700  $\mu\text{C}/\text{cm}^2$ .
- Develop the top resist layer A-RP using o-xylene developer for 30 s.
- Develop the bottom resist layer COPEL6 using o-xylene developer for 40 s.
- Remove exposed graphene using 1.5 min of oxygen plasma ashing. 50 W, 250 mT chamber pressure and 10 sccm flow of oxygen.
- Remove remaining resist using acetone.
- Rinse with isopropanol.
- Dry using nitrogen gas.

## A.3 Chemical Doping

### A.3.1 Dopant blend

The standard dopant blend consisting of F4TCNQ molecules mixed with PMMA is made using the following recipe:

- 25 mg of dry F4TCNQ powder is mixed with 3 mL of anisole. This solution is referred to as ‘X’.
- 0.5 mL of X is mixed with 1 mL of PMMA A6 (PMMA, 6 wt. % in anisole), yielding the final dopant blend.

### A.3.2 Spin coating

Standard application process of the standard dopant blend to yield charge neutral graphene:

- Spin coat P(MMA-MAA 8.5 %), 6 wt. % in ethyl lactate solvent (COPEL6). At 6,000 rpm for 1 min, the resulting thickness is  $\approx$  100 nm. This is the spacer layer
- Bake for 5 min at 160 °C.
- Spin coat dopant blend. At 6,000 rpm for 1 min, the resulting thickness is  $\approx$  150 nm.

- Bake for 5 min at 160 °C (Baking time is related to final doping level, and can be changed as needed).

## References

- [1] S. Lara-Avila et al. Non-volatile photochemical gating of an epitaxial graphene/polymer heterostructure. *Advanced Materials* **23**.7 (2011), 878–882.
- [2] A. Lartsev et al. Tuning carrier density across Dirac point in epitaxial graphene on SiC by corona discharge. *Applied Physics Letters* **105**.6 (2014), 063106.
- [3] D. Waldmann et al. Bottom-gated epitaxial graphene. *Nature Materials* **10**.5 (2011), 357–360.
- [4] J. Xue et al. Scanning tunnelling microscopy and spectroscopy of ultra-flat graphene on hexagonal boron nitride. *Nature Materials* **10** (2011).
- [5] A. S. Mayorov et al. How Close Can One Approach the Dirac Point in Graphene Experimentally? *Nano Letters* **12**.9 (2012), 4629–4634.
- [6] A. S. Mayorov et al. Micrometer-Scale Ballistic Transport in Encapsulated Graphene at Room Temperature. *Nano Letters* **11**.6 (2011), 2396–2399.
- [7] R. R. Nair et al. Fine structure constant defines visual transparency of graphene. *Science (New York, N.Y.)* **320**.5881 (2008), 1308.
- [8] A. A. Balandin. Thermal properties of graphene and nanostructured carbon materials. *Nature Materials* **10**.8 (2011), 569–581.
- [9] C. Lee et al. Measurement of the elastic properties and intrinsic strength of monolayer graphene. *Science (New York, N.Y.)* **321**.5887 (2008), 385–8.
- [10] P. R. Wallace. The band theory of graphite. *Physical Review* **71**.9 (1947), 622–634.
- [11] K. S.K. S. Novoselov et al. Electric field effect in atomically thin carbon films. *Science* **306**.5696 (2004), 666–669.
- [12] K. S. Novoselov et al. Two-dimensional gas of massless Dirac fermions in graphene. *Nature* **438**.7065 (2005), 197–200.
- [13] K. v. Klitzing et al. New Method for High-Accuracy Determination of the Fine-Structure Constant Based on Quantized Hall Resistance. *Physical Review Letters* **45**.6 (1980), 494–497.
- [14] T. J. B M Janssen et al. Graphene, universality of the quantum Hall effect and redefinition of the SI system universality of the quantum Hall effect and redefinition of the SI system New Journal of Physics Graphene, universality of the quantum Hall effect and redefinition of the SI system. *New Journal of Physics* **9**.13 (2011), 93026–93026.
- [15] A. Tzalenchuk et al. Towards a quantum resistance standard based on epitaxial graphene. *Nature nanotechnology* **5**.3 (2010), 186–9.
- [16] R. Ribeiro-Palau et al. Quantum Hall resistance standard in graphene devices under relaxed experimental conditions. *Nature Nanotechnology* **10**.September (2015), 1–18.
- [17] T. J.B. M. Janssen et al. Operation of graphene quantum Hall resistance standard in a cryogen-free table-top system. *2D Materials* **2**.3 (2015), 035015.

- [18] J. A. Alexander-Webber et al. Giant quantum Hall plateaus generated by charge transfer in epitaxial graphene. *Scientific Reports* **6**.May (2016), 30296.
- [19] C. Virojanadara et al. Homogeneous large-area graphene layer growth on 6H-SiC(0001). *Physical Review B* **78**.24 (2008), 245403.
- [20] S. Kopylov et al. Charge transfer between epitaxial graphene and silicon carbide. *Applied Physics Letters* **97**.11 (2010).
- [21] M Yang et al. Puddle-Induced Resistance Oscillations in the Breakdown of the Graphene Quantum Hall Effect. *Physical Review Letters* **117**.23 (2016).
- [22] S. Cho et al. Charge transport and inhomogeneity near the minimum conductivity point in graphene. *Physical Review B - Condensed Matter and Materials Physics* **77**.8 (2008).
- [23] C Coletti et al. Charge neutrality and band-gap tuning of epitaxial graphene on SiC by molecular doping. *Physical Review B - Condensed Matter and Materials Physics* **81**.23 (2010).
- [24] J. Jobst et al. Quantum oscillations and quantum Hall effect in epitaxial graphene. *Physical Review B* **81**.19 (2010), 195434.
- [25] S. Datta et al. *Quantum Transport: Atom to Transistor*. Cambridge University Press, 2005.
- [26] S. Datta. *Electronic Transport in Mesoscopic Systems*. Cambridge Studies in Semiconductor Physi. Cambridge University Press, 1997.
- [27] M. Katsnelson et al. *Graphene: Carbon in Two Dimensions*. Cambridge University Press, 2012.
- [28] H. Aoki et al. *Physics of Graphene*. NanoScience and Technology. Springer International Publishing, 2013.
- [29] E. Malic et al. *Graphene and Carbon Nanotubes: Ultrafast Optics and Relaxation Dynamics*. Wiley, 2013.
- [30] E. M. Lifshits et al. Theory of the Shubnikov-de Haas effect. *Journal of Physics and Chemistry of Solids* **4**.1-2 (1958), 1–10.
- [31] R. Kundu. Tight-binding parameters for graphene. *Modern Physics Letters B* **25**.03 (2011), 163–173.
- [32] J. Huang et al. Disorder induced Dirac-point physics in epitaxial graphene from temperature-dependent magneto-transport measurements. *Physical Review B* **075407** (2015), 6.
- [33] Y. Zhang et al. Origin of spatial charge inhomogeneity in graphene. *Nature Physics* **6**.1 (2010), 74–74.
- [34] Q. Li et al. Disorder-induced temperature-dependent transport in graphene: Puddles, impurities, activation, and diffusion. *Physical Review B - Condensed Matter and Materials Physics* **84**.11 (2011).
- [35] I. A. LuK'Yanchuk et al. Phase analysis of quantum oscillations in graphite. *Physical Review Letters* **93**.16 (2004).
- [36] K. S. Novoselov et al. Room-temperature quantum hall effect in graphene. *Science* **315**.5817 (2007), 1379.
- [37] C. Riedl et al. Quasi-Free-Standing Epitaxial Graphene on SiC Obtained by Hydrogen Intercalation. *Physical Review Letters* **103**.24 (2009), 246804.

- [38] W. A. D. Heer et al. Large area and structured epitaxial graphene produced by confinement controlled sublimation of silicon carbide (2011).
- [39] T. Yager et al. Express optical analysis of epitaxial graphene on SiC: Impact of morphology on quantum transport. *Nano Letters* **13**.9 (2013), 4217–4223.
- [40] V. Panchal et al. Standardization of surface potential measurements of graphene domains. *Scientific reports* **3**.2 (2013), 2597.
- [41] A. C. Ferrari et al. Raman spectroscopy as a versatile tool for studying the properties of graphene. *Nature Nanotechnology* **8**.4 (2013), 235–246.
- [42] J. Rohrl et al. Raman spectra of epitaxial graphene on SiC(0001). *Applied Physics Letters* **92**.20 (2008), 201918.
- [43] B Jeckelmann et al. The quantum Hall effect as an electrical resistance standard. *Rep. Prog. Phys* **64** (2001), 1603–1655.
- [44] J. M. Williams et al. An automated cryogenic current comparator resistance ratio bridge for routine resistance measurements. *Metrologia* **47**.3 (2010), 167–174.
- [45] W. Chen et al. Surface Transfer p-Type Doping of Epitaxial Graphene. *Journal of the American Chemical Society* **129**.34 (2007), 10418–10422.
- [46] H.-Z. Tsai et al. Molecular Self-Assembly in a Poorly Screened Environment: F 4 TCNQ on Graphene/BN. *ACS Nano* **9**.12 (2015), 12168–12173.
- [47] J. Li et al. Measurement of Small Molecular Dopant F4TCNQ and C60F36 Diffusion in Organic Bilayer Architectures. *ACS Applied Materials and Interfaces* **7**.51 (2015), 28420–28428.
- [48] I. E. Jacobs et al. *Controlling Molecular Doping in Organic Semiconductors*. 2017.
- [49] P Pingel et al. Comprehensive picture of p-type doping of P3HT with the molecular acceptor F 4 TCNQ. *PHYSICAL REVIEW B* **87**.73 (2013).
- [50] J. Li et al. Quantitative Measurements of the Temperature-Dependent Microscopic and Macroscopic Dynamics of a Molecular Dopant in a Conjugated Polymer. *Macromolecules* **50**.14 (2017), 5476–5489.
- [51] J. Crank et al. *The Mathematics of Diffusion*. Oxford science publications. Clarendon Press, 1979.
- [52] A. Kumar et al. Charge-Transfer-Driven Nonplanar Adsorption of F 4 TCNQ Molecules on Epitaxial Graphene. *ACS Nano* **11**.5 (2017), acsnano.7b01599.
- [53] M. Knap et al. Transport in two-dimensional disordered semimetals. *Physical Review Letters* **113**.18 (2014), 1–5.
- [54] J. Ping et al. Disorder-induced magnetoresistance in a two-dimensional electron system. *Physical Review Letters* **113**.4 (2014), 1–5.
- [55] R. P. Tiwari et al. Model for the magnetoresistance and Hall coefficient of inhomogeneous graphene. *Physical Review B - Condensed Matter and Materials Physics* **79**.16 (2009), 1–7.
- [56] J. M. Poumirol et al. Electron-hole coexistence in disordered graphene probed by high-field magneto-transport. *New Journal of Physics* **12**.8 (2010), 083006.
- [57] J. Yan et al. Correlated charged impurity scattering in graphene. *Physical Review Letters* **107**.20 (2011).
- [58] Q. Li et al. Theory of 2D transport in graphene for correlated disorder. *Physical Review Letters* **107**.15 (2011).

- [59] L. A. Ponomarenko et al. Tunable metal–insulator transition in double-layer graphene heterostructures. *Nature Physics* **7** (2011).
- [60] H. Ishiwara et al. *Ferroelectric Random Access Memories: Fundamentals and Applications*. Topics in Applied Physics. Springer, 2004.
- [61] D. W. Allan. Should the Classical Variance Be Used As a Basic Measure in Standards Metrology? *IEEE Transactions on Instrumentation and Measurement* **IM-36.2** (1987), 646–654.
- [62] C. Cervetti et al. The classical and quantum dynamics of molecular spins on graphene. *Nature Materials* **15.2** (2016), 164–168.
- [63] M. Garnica et al. Long-range magnetic order in a purely organic 2D layer adsorbed on epitaxial graphene. *Nature Physics* **9.6** (2013), 368–374.
- [64] H. He et al. Fabrication of graphene quantum hall resistance standard in a cryogenic-table-top system. *2016 Conference on Precision Electromagnetic Measurements (CPEM 2016)* (2016), 1–2.
- [65] H. He et al. Uniform doping of graphene close to the charge neutrality point by polymer-assisted spontaneous assembly of molecular dopants. *Manuscript under consideration in Nature Materials* (2018), arXiv:1805.05644.

